Chapter 9
Solar- and Visible-Blind AlGaN Photodetectors

Moritz Brendel, Enrico Pertzsch, Vera Abrosimova, Torsten Trenkler and Markus Weyers

Abstract This chapter presents an overview on UV photodetectors based on the $Al_xGa_{1-x}N$ material system. After an introduction into the field of UV photodetection and material-related issues, the main physics, the operation principles, and characteristic parameters of the most popular photodetector device types will be briefly addressed including the photoconductor, the Schottky barrier diode, the metal–semiconductor–metal structure, the p-i-n diode, the avalanche detector as well as the phototube and the photomultiplier tube. Further, scientific results on $Al_xGa_{1-x}N$-based photodetectors are compiled in order to illustrate the potential of the different photodetector device types for a wide range of UV applications. And finally, the state-of-the-art of commercially available photodetectors for UV detection and monitoring is discussed.

9.1 Introduction

The ultraviolet (UV) portion of the electromagnetic spectrum, i.e., electromagnetic radiation in the wavelength range between 400 and 10 nm, is divided into several subranges, e.g., UV-A (380–315 nm), UV-B (315–280 nm), UV-C (280–200 nm),

---

M. Brendel (✉) · M. Weyers
Ferdinand-Braun-Institut, Leibniz-Institut für Höchstfrequenztechnik, Gustav-Kirchhoff-Str. 4, 12489 Berlin, Germany
e-mail: moritz.brendel@fbh-berlin.de

M. Weyers
e-mail: markus.weyers@fbh-berlin.de

E. Pertzsch · V. Abrosimova · T. Trenkler
JENOPTIK Polymer Systems GmbH, Köpenicker Strasse 325b, 12555 Berlin, Germany
e-mail: enrico.pertzsch@jenoptik.com

V. Abrosimova
e-mail: vera.abrosimova@jenoptik.com

T. Trenkler
e-mail: torsten.trenkler@jenoptik.com

M. Kneissl and J. Rass (eds.), *III-Nitride Ultraviolet Emitters*,
Springer Series in Materials Science 227, DOI 10.1007/978-3-319-24100-5_9

and VUV (200–10 nm),[1] which help to classify optoelectronic devices, i.e., emitters and detectors, by their operational range. A photodetector (PD)[2] sensitive only in the UV range thus can be visible-blind or even solar-blind whenever detection capability is limited to wavelengths below 380 or 280 nm, respectively. Application fields for such devices in industry, military, medicine, and science include UV dosimetry, flame sensing, non-line-of-sight communication and biological as well as chemical sensing. Some specific examples are

- UV lithography (193 nm)
- UV curing of paints, adhesives, compounds, and polyester plastics (e.g., 365 nm)
- Disinfection of water, air, and surfaces (240–290 nm)
- Detection of corona discharges (<280 nm)
- Missile plume detection and combustion engine control
- Chemical and biological threat detection
- UV spectroscopy
- UV astronomy.

As an example, UV-C lamps for water and air disinfection have to be monitored in order to detect failure and to ensure the required UV-C dose. As long as mercury medium pressure lamps are used in such systems,[3] for an accurate measurement of the UV-C dose of the 254 nm line, the parasitic UV-A and UV-B emission has to be excluded. Similar examples are the imaging of corona discharges at broken transmission lines or of missile plume and other launching actions, which are usually against a daylight background within the earth's atmosphere. III–V semiconductor materials bearing the possibility to design the spectral properties of a PD accordingly, without the use of an external spectral filter, that is costly and tends to age under UV radiation, are favorable in such applications.

The ternary $Al_xGa_{1-x}N$ material system spans a range of bandgap energies between those values for the binaries GaN with 3.5 eV and AlN with 6.2 eV [1], covering band edge cut-offs between about 360 and 200 nm, respectively. AlGaN-based PDs are visible-blind and solar blindness can be tuned via the Al mole fraction with $x_{\mathrm{Al}} \geq 0.45$, where alternative materials, such as Si, GaAs, GaP, and SiC are not intrinsically blind to visible portions of the spectrum. Radiation hardness and the capability to withstand high-thermal stress due to the wide direct energy gap put the AlGaN system in favor for its usage in a number of UV applications. High values for spontaneous polarization along the c-axis of the wurtzite cell as well as a strain-dependent piezoelectric polarization have to be considered, since both affect the optical and electrical properties of III-nitride devices consisting of heterojunctions [1]. However, with increasing Al content

---

[1] VUV: vacuum UV.

[2] The abbreviation PD will be used for *photodetector* and *photodiode* throughout the text.

[3] Hg-lamps deliver the required intensities between 10^{-4} to 0.1 W cm^{-2}, where UVC-LEDs with an output of 10^{-4} W cm^{-2} are commercially available but are still too weak for water disinfection.

several difficulties had to be dealt with during the past two decades of UV photodetector development.

- First of all, due to the tensile strain resulting from lattice and thermal mismatch, the heteroepitaxial growth of an $Al_xGa_{1-x}N$ layer of a certain thickness directly on a GaN/sapphire template is limited to AlN mole fractions below about 30 % before cracking of the layers occurs (see e.g., [2] and references therein). Material defects, such as stacking faults, threading dislocations and grain boundaries are usually known to deteriorate the performance of any optoelectronic device. Several approaches to grow high-quality $Al_xGa_{1-x}N$ material have been reported, e.g., the use of low-temperature (LT) AlN buffer layers [3], superlattices of GaN/AlN [4], GaN/AlGaN, and AlN/AlGaN [5] layers and different epitaxial lateral overgrowth techniques [6–8]. Anyway, in terms of back-illuminated PDs, the substrate as well as the buffer layers may limit the short-wavelength performance due to the onset of absorption, hence the material should be chosen reasonably.
- Another major issue is the p-type conductivity of $Al_xGa_{1-x}N$ layers. Doping of GaN with Mg introduces a shallow acceptor level of the substitutional magnesium on a gallium lattice site Mg_{Ga} with an ionization energy of 200 meV [9]. But due to the passivation of incorporated Mg by hydrogen, a post-growth annealing step at temperature above 600 °C is necessary to obtain conductive p-type GaN:Mg [10, 11]. Maximum hole concentration of about 10^{18} cm^3 for Mg concentration of about 3.3×10^{19} cm^3 can be achieved [12], and a further increase of the Mg concentration leads to a subsequent decrease of the free-hole concentration since the Mg_{Ga} acceptor is expected to self-compensate via the nitrogen vacancy V_N^{3+} [13, 14]. With increasing x_{Al}, the ionization energy of the magnesium acceptor level also increases up to 0.51 eV in AlN [15, 16] resulting in a strongly reduced concentration of free holes in AlN:Mg compared to GaN: Mg for the same net acceptor concentration.
- Last but not least, the development of proper ohmic contacts to both n- and p-type $Al_xGa_{1-x}N$ layers as well as the formation of non-leaky Schottky-type metal-$Al_xGa_{1-x}N$ junctions are not straight forward. The main issue concerning ohmic contacts is the absence of a metal with sufficient work function, so that a thermal annealing step after the metallization is necessary to obtain ohmic behavior of the respective metal-$Al_xGa_{1-x}N$ junction. For an n-GaN layer, this can be done using Ti/Al layers annealed at 900 °C for 20–30 s and for a p-GaN layer by annealing Ni/Au for 30 s at 700 °C [17, 18]. These examples illustrate that devices with n-type as well as p-type ohmic contacts need two different process steps for contact formation due to the differences in annealing temperature and time. From the above–mentioned, it seems that Schottky barriers to the $Al_xGa_{1-x}N$ material—with barrier heights between 0.1 eV using Ti and more than 1.1 eV for Pt—would be easily produced by just leaving out the annealing step. But also a proper surface treatment prior to metallization, e.g., removing native oxides by N_2^+ ion sputtering [19] or HCl wet etching [20], has to be ensured for the desired metal-$Al_xGa_{1-x}N$ combination. Dependent on the metal

> used the thermal stability of Schottky contacts is limited since above where annealing effects set in the electrical behavior of the contact changes. Thus, it is necessary to arrange the process flow accordingly, i.e., any ohmic formation needs to be done prior to a Schottky metallization and the thermal range of device operation must be chosen reasonably. Since a number of metals have already been used to process the ohmic as well as the Schottky contacts, the interested reader is referred to the comprehensive review article of Pearton et al. [21].

However, during the last two decades, many research groups have developed different strategies to deal with those difficulties. Although a number of review articles on III-Nitride UV photodetectors have already been published (e.g., [22–28]), a summarized view on the development of some device types will be presented and various approaches to achieve high-performance devices will be addressed in this chapter.

9.2 Basics of Photodetectors

In this section, the relevant basics about photodetectors will be introduced. After a part covering physical essentials of photodetection, the structural and operational principles of certain photodetector types are presented. We emphasize here that this collection is based on several contributions from the literature to which the reader is referred for deeper insights into the matter, e.g., [29–35]. A complete coverage is not possible here due to the limited space. Nevertheless, a sufficient backbone should be available after the study of this section, in order to handle the more material and research-related parts that follow in Sect. 9.3.

9.2.1 Characteristic Parameters and Phenomena

The main physical parameters that determine the properties of a photodetector (PD), such as optical properties, quantum efficiency and responsivity, rise and fall times, linearity as well as noise properties, will be introduced.

9.2.1.1 Optical Properties of Semiconductors

The dielectric function of a solid determines its optical constants, i.e., its refractive index n_{ref} and extinction coefficient κ. On the one hand, these quantities define the reflected portion R_{ji} (see Fig. 9.1a) of an optical signal of power $P_j(\lambda)$ incident on a material i with n_i and κ_i within a medium j with n_j and $\kappa_j = 0$ [36]

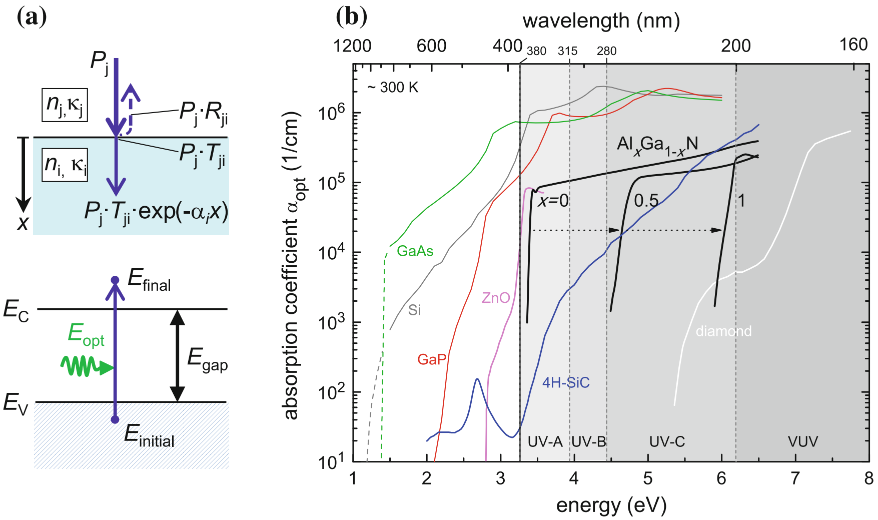

Fig. 9.1 **a** (*Top*) Beam propagates through medium *j*, impinges on surface of material *i* and is attenuated within material *i* due to absorption, (*bottom*) schematic of fundamental band-to-band absorption process. **b** Optical absorption coefficient α_{opt} for various semiconductors (Si: dashed [35] full [37], GaAs: dashed [38] full [37], GaP [37], 4H–SiC [39], ZnO [40], AlGaN [41], diamond [42, 43])—for further explanation see text and footnote 5

$$R_{ji} = \frac{(n_i - n_j)^2 + \kappa_i^2}{(n_i + n_j)^2 + \kappa_i^2}, \tag{9.1}$$

where all quantities depend on the optical wavelength λ of the incident photons.[4] Thus, only the portion $T_{ji} = 1 - R_{ji}$ of P_j is transmitted into the medium *i*. On the other hand, the optical absorption coefficient $\alpha_{opt,i}(\lambda) = 4\pi\kappa_i(\lambda)/\lambda$ determines the number of photogenerated free charges—i.e., electron–hole pairs—and gives a measure of attenuation of the optical power *P* along the distance *x* according to Lambert-Beers law $P(x) \propto \exp(-\alpha x)$. Considering the fundamental band-to-band absorption process, shown in the bottom image of Fig. 9.1a, i.e., intrinsic excitation of electrons from the filled valence band states with energies $E_{initial} \leq E_V$ to the empty conduction band states with $E_{final} \geq E_C$, a threshold wavelength $\lambda_{thr} \leq hc/E_{gap}$ for photoabsorption can be derived, where *h* is Plancks constant, *c* is the vacuum velocity for electromagnetic radiation and $E_{gap} = E_C - E_V$ is the direct or indirect bandgap energy of the material. By further neglecting absorption processes from or to energy levels within the bandgap, λ_{thr} therefore defines the wavelength range of the material suitable for photodetection. Figure 9.1b summarizes spectra of α_{opt} at about room temperature for various indirect (Si, GaP, SiC,

---

[4] This (λ)-dependence will sometimes be omitted for the sake of clarity.

and diamond) as well as direct (GaAs, ZnO, and AlGaN) semiconductor materials suitable to fabricate photodetectors with λ_{thr} ranging from the near infra-red (NIR) to the UV-C region.[5] Si, GaAs, and GaP show relatively high values of $\alpha_{\mathrm{opt}} \geq 10^3\ \mathrm{cm}^{-1}$ for wavelengths above 380 nm, unlike the wide bandgap materials ZnO, SiC, $Al_xGa_{1-x}N$, and diamond, which thus are attractive alternatives for visible-blind or solar-blind photodetection.

9.2.1.2 Quantum Efficiency and Responsivity

The quantum efficiency (QE) of a photodetector, also called the external quantum efficiency (EQE), is an experimentally accessible quantity. It is given by the ratio of electric charge measured in an external circuit and the number of incident photons upon illumination on the active area. Thus, it can directly be determined via measurement of the device photocurrent $I_{\mathrm{photo}}(\lambda)$ when the optical power $P_{\mathrm{opt}}(\lambda)$ of the incident photons with energy $E_{\mathrm{opt}}(\lambda)$ is known [31]

$$\eta_{\mathrm{ext}}(\lambda) = \frac{\#\,\text{charge measured}}{\#\,\text{photons incident}} = \frac{I_{\mathrm{photo}}(\lambda)/q}{P_{\mathrm{opt}}(\lambda)/E_{\mathrm{opt}}(\lambda)}, \tag{9.2}$$

where q is the elementary charge. In order to relate η_{ext} to the underlying physical processes in a device, the theoretical approach put forward by Geist in [33] is helpful, where the EQE for normal incidence is given by

$$\eta_{\mathrm{ext}}(\lambda) = T_{\mathrm{opt}}(\lambda) \cdot Y(\lambda) \cdot CE(\lambda) = T_{\mathrm{opt}} \cdot \eta_{\mathrm{int}} \tag{9.3}$$

with T_{opt} the fraction of power transmitted into the photodetector, Y the quantum yield, CE the collection efficiency, and η_{int} the internal quantum efficiency (IQE), accounting for the recombination losses only by giving the ratio of electron–hole pairs created and photons absorbed within the device. As long as free-carrier absorption or impact ionization is negligible, the quantum yield is $Y \approx 1$. The collection efficiency CE accounts for structural and electrical properties (carrier sweep-out) as well as for optical properties (optical absorption) of a certain photodetector device and it can be calculated by integration of

$$CE = \int \alpha_{\mathrm{opt}} \cdot \exp\left[-\alpha_{\mathrm{opt}} \cdot x\right] \cdot P(x)\mathrm{d}x \tag{9.4}$$

over the whole device along x (c.f. Fig. 9.2a). $P(x)$ describes the carrier collection probability and can be approximated by drift-diffusion modeling [33]. As a rule of thumb, $P(x)$ is high (→ 1) where photogenerated carriers are either drifting or are

---

[5] Data of α_{opt} was either directly extracted from the literature (*tabular*: Si, GaAs, GaP [37] or *plot-digitized*: Si [35], SiC [39], diamond [42], GaAs [38], ZnO [40]) or calculated from the dielectric function (all digitized: diamond [43], AlGaN [41]).

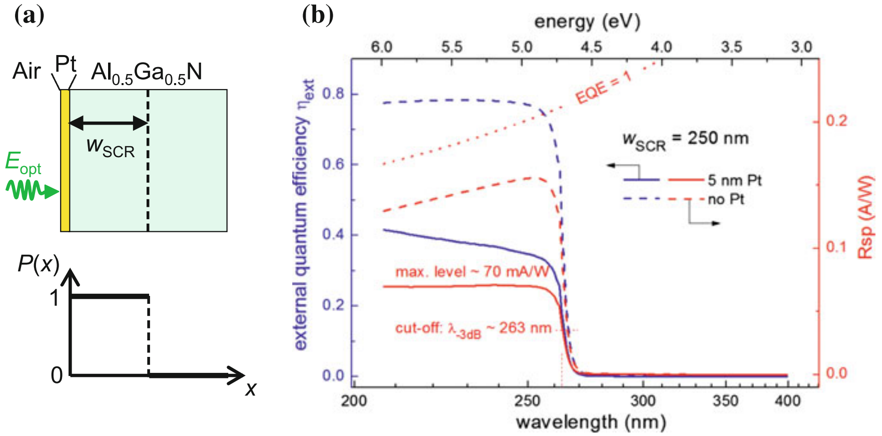

Fig. 9.2 **a** Cross-sectional schematic (*top*) of a Pt/n-$Al_{0.5}Ga_{0.5}N$ Schottky barrier PD as well as a possible collection efficiency probability $P(x)$ (*bottom*) within the device. **b** The calculated EQE (*blue*) and responsivity (*red*) for finite (*full*) and zero (*dashed*) Pt-layer thickness

subject to diffusion into field regions, and it is low (→ 0) where recombination losses become dominant.

Referring to the cross-section of a simplified Pt/n-$Al_{0.5}Ga_{0.5}N$ Schottky barrier photodetector[6] irradiated from the Pt-side, as shown in Fig. 9.2a, the EQE can be estimated utilizing (9.3) and (9.4) as follows:

1. When the optical constants n_{ref} and κ of all materials involved are known,[7] the optical transmission in (9.3) can be estimated by

$$T_{\mathrm{opt}} = (1 - R_{\mathrm{air-Pt}}) \cdot \exp(-\alpha_{\mathrm{Pt}} \cdot t_{\mathrm{Pt}}) \cdot (1 - R_{\mathrm{Pt-AlGaN}}), \qquad (9.5)$$

   where the R_{ji} are calculated from (9.1) and the exponential factor accounts for attenuation within the Pt-layer of $t_{\mathrm{Pt}} = 5$ nm thickness. Multiple reflections in any layer are neglected.
2. Assuming, that the photogenerated carriers within the space charge region (SCR) of width $w_{\mathrm{SCR}} = 250$ nm in the n-type $Al_{0.5}Ga_{0.5}N$-layer will all be collected, the carrier collection probability writes

$$P(x) = \begin{cases} 1 & \text{within } w_{\mathrm{SCR}} \\ 0 & \text{elsewhere.} \end{cases} \qquad (9.6)$$

   This is illustrated in the bottom image of Fig. 9.2a.

---

[6] A more detailed description of that type of PD will be given below.

[7] Data for n and κ in this example are taken from [44] for Pt and have been derived from the dielectric function given in [41] for $Al_{0.5}Ga_{0.5}N$.

3. The resulting spectral shape of the EQE for the example PD can be calculated as

$$\eta_{\mathrm{ext}} = T_{\mathrm{opt}} \cdot \left(1 - \exp(-\alpha_{\mathrm{opt}} \cdot w_{\mathrm{SCR}})\right), \tag{9.7}$$

   which is plotted in Fig. 9.2b (blue lines, left axis).

The onset of absorption results in an increase in EQE for wavelengths below about 270 nm. The influence of the optical properties of the Pt-layer, especially its reflectance, on the EQE is evident when comparing the strongly reduced EQE (full line) with that for the hypothetical case without the Pt-layer (dashed line), where $R_{\mathrm{air-Pt}}, t_{\mathrm{Pt}} \rightarrow 0$ and $R_{\mathrm{Pt-AlGaN}} \rightarrow R_{\mathrm{air-AlGaN}}$. Further, recombination losses at the surface, in the bulk, and at the contacts may reduce CE and thus lower the EQE significantly. Anyway, the main restriction to the validity of (9.2) is a linear relationship between the photocurrent I_{photo} and the optical power P_{opt}

$$I_{\mathrm{photo}} = Rsp \cdot P_{\mathrm{opt}} \quad \Leftrightarrow \quad Rsp(\lambda) = \frac{I_{\mathrm{photo}}(\lambda)}{P_{\mathrm{opt}}(\lambda)} \tag{9.8}$$

with $Rsp(\lambda)$ the responsivity, which is the most fundamental figure-of-merit in practice to describe a detectors capability to convert an optical signal measured in Watt into an electric current signal measured in Ampère. When combining (9.2) and (9.8), the responsivity is related to the EQE via

$$Rsp(\lambda) = \eta_{\mathrm{ext}}(\lambda) \cdot \frac{q}{E_{\mathrm{phot}}(\lambda)}. \tag{9.9}$$

The resulting responsivity of the example PD is also plotted in Fig. 9.2b (red lines, right axis) and the explanations made above for the EQE translate into this responsivity spectrum, accordingly. But concerning the optical properties of the Pt-layer, besides a reduction of the absolute Rsp, it can be seen that the presence of the semitransparent Pt-layer alters the spectral shape from rather flat to increasing with wavelength, until the Rsp suddenly drops for $\lambda > 255$ nm (the $Rsp(EQE = 1)$ line has been introduced for comparison).

A cut-off wavelength λ_{co} is often defined to serve as a spectral measure indicating the operation wavelength range of a photodetector. This spectral cut-off is defined as the wavelength where the responsivity drops to a certain value, e.g., 50 or 10 %, of its maximum value toward long wavelengths. Just as the threshold wavelength λ_{thr}, it directly corresponds to the onset of absorption and is thus related to the bandgap energy. The 50 % cut-off wavelength in Fig. 9.2 is 263 nm, indicating a solar-blind operation range for this Pt/$\mathrm{Al_{0.5}Ga_{0.5}N}$ Schottky barrier PD.

9.2.1.3 Rise and Fall Times

The response time for a certain change in measured electrical signal—current or voltage—upon a change in the incident optical signal intensity is of importance for photodetection applications. Practically, the rise time τ_{rise} from the dark signal to 90 % of maximum signal upon illumination and the fall time τ_{fall} to 10 %, as shown in Fig. 9.3a, are the common parameters used for device specification. These time constants are influenced by several factors which are related to the material properties, the photodetector structure, and the output circuitry. To illustrate these relations, we refer to the p-i-n diode structure shown in Fig. 9.3a.[8] The equivalent circuit parameters of a photodiode are illustrated in Fig. 9.3b. According to (9.2), the static response of a photodiode can be viewed as a photocurrent I_p generated upon illumination due to the optical signal of power P_{opt}. This current source is in parallel with the rectifying diode junction and the reverse bias-dependent diode capacitance C_D of the junction. A series resistance R_S, in the order of a few Ohms, accounts for the resistance due to ohmic contacts and the bulk material. Parasitic inductances in series to R_S, e.g., due to wire lines, and parasitic capacitors in parallel to C_D, e.g., due to bond pads, as well as the parallel shunt resistance of the junction, which is usually >10^7, are neglected. From that, a low-pass filter behavior of the photodiode response—current or voltage—upon a modulated incident signal can be expected. Hence, the dependence of the responsivity *Rsp* on the signal modulation frequency *f* is approximated by [31]

$$Rsp(f) = \frac{Rsp_0}{\sqrt{1 + (f/f_{\text{co}})^2}}, \quad \text{where} \quad f_{\text{co}} = \frac{1}{2\pi\tau_r} \tag{9.10}$$

with Rsp_0 the static responsivity and f_{co} the cut-off frequency, also referred to as the bandwidth of the photodiode. This behavior is shown in Fig. 9.3c for the case of $f_{\text{co}} = 3$ MHz. The cut-off frequency measures the capability of the photodetector to follow a frequency-modulated input signal,[9] and it is determined by the response time τ_r, which depends on different contributions:

- The drift of photo-excited carriers in high-field regions, i.e., the i-layer, of the device. The respective response time τ_{tr} is set by the field-dependent carrier transit time t_{tr} and can be approximated by [31]

$$\tau_{\text{tr}} \approx 0.36 \cdot t_{\text{tr}}, \quad \text{where} \quad t_{\text{tr}} = w_{\text{SCR}}/(\mu \cdot F) \tag{9.11}$$

---

[8] A more detailed description of that type of PD will be given below.

[9] After (9.10) the responsivity drops by a factor of $1/\sqrt{2}$ at the bandwidth f_{co}, which corresponds to a decrease in power level of −3 dB (∼−1/2). Therefore, f_{co} is also called the 3 dB-bandwidth $f_{3\text{dB}}$.

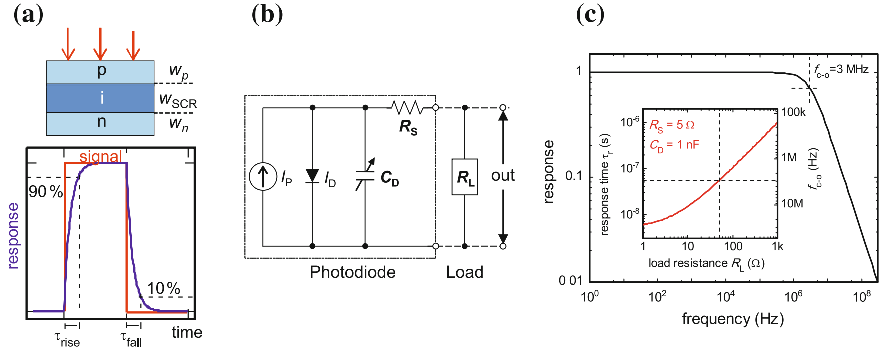

Fig. 9.3 **a** The schematic layer structure (*top*) of a p-i-n diode, rise time τ_{rise} and fall time τ_{fall} (*bottom*) of the system response upon signal change. **b** Equivalent circuit of a photodiode with readout (simplified, see text). **c** Low-pass output characteristics of a photodiode response upon a frequency-modulated input light signal—inset shows dependency of the response time (*left axis*) and thus the cut-off frequency (*right axis*) on the load resistance

with w_{SCR} the width of the space charge region, μ the mobility of the traveling carriers and F the electric field strength. Thus this contribution can be adjusted by the depletion layer width and the applied bias.

- Diffusion of photo-excited minority carriers in field-free regions, i.e., the p- and n-regions: The diffusion time before recombination τ_{diff} is given by the minority carrier lifetime τ_{rec} via [31]

$$\tau_{\text{diff}} \approx \frac{w^2}{2D}, \quad \text{where} \quad D = L^2/\tau_{\text{rec}} \tag{9.12}$$

with w the length of the field-free region, D the diffusion constant, and L the corresponding diffusion length.[10] This contribution to the response time is reduced when w is as small as possible and D is sufficiently large.

- The combination of the load resistance R_{L} to read out the detector signal, the diode series resistance R_{S}, and the junction capacitance C_{D} leads to a RC-time constant τ_{RC} given by

$$\tau_{\text{RC}} = (R_{\text{S}} + R_{\text{L}}) \cdot C_{\text{D}} \tag{9.13}$$

that limits the bandwidth. A reduction of R_S and of C_D lowers this contribution. Since $C_D \sim A/w_{\text{SCR}}$ with A the junction area, the diode capacitance is lowered for a small junction area and a wide space charge region.

---

[10] D and L refer to *minority* carrier values, e.g., electrons with D_n and L_n in a p-type region of width w_p.

The total response time τ_r, i.e., rise or fall time, is then estimated as

$$\tau_r = \sqrt{\tau_{tr}^2 + \tau_{diff}^2 + \tau_{RC}^2}, \tag{9.14}$$

where the contributions of τ_{tr} and τ_{diff}, and τ_{RC} can be altered by device geometry and material properties to match the application requirements. In the inset of Fig. 9.3c, the dependence of the response time τ_r on the load resistance R_L is shown for 5 Ω series resistance, 1 nF junction capacitance, and vanishing contributions of τ_{tr} and τ_{diff}. The cut-off $f_{co} = 3$ MHz can be achieved with a load resistance of 50 Ω and a further reduction in τ_r is possible for even smaller R_L.

A closer look on the recombination lifetime τ_{rec} of excess carriers, which contributes to the response time τ_r, is possible by a simple theoretical analysis of temporal changes in the photo-induced free-carrier enhancement $\Delta n(t)$ [29]. Considering mono-molecular recombination processes only, exponential terms of the form $\Delta n(t) \sim \left[1 - \exp(-t/\tau_{growth})\right]$ for signal growth and $\Delta n(t) \sim \exp(-t/\tau_{decay})$ for signal decay result, which are easy to interpret by means of the respective time constants[11] [29, 32]. When regarding trapping processes in such an analysis, more complex terms for $\Delta n(t)$ then can be approximated which may be used to fit experimental data—see e.g., the summarizing table given in Sect. 9.2 in Bube [29]. Generally, deep centers with certain capture cross sections for mobile carriers have been found to cause long lifetimes in transient processes—see also the following paragraph. Additionally, carrier trapping processes are dependent on external or internal electrical fields and on temperature. Therefore, unpredictable instabilities may occur during operation, deteriorating the performance of a photodetector in applications utilizing modulated radiation sources.

9.2.1.4 Persistent Photoconductivity (PPC)

Rise and fall times of an optically excited system in excess of several 1000 s have been reported for many different poly- and single-crystalline semiconductor materials as well as alloys since Kohlrausch examined the residual discharge of a Leyden jar in 1854 [45]. This phenomenon is commonly termed persistent photoconductivity (PPC) and manifests itself in the transient build-up and decay of a photo-induced current, which is often found to be well described by a stretched exponential of the form $I(t) \sim \exp\left[(-t/\tau)^{\beta}\right]$, where τ is a constant with the dimensions of time and $0 < \beta \le 1$ is the Kohlrausch stretching parameter, which accounts for the microscopic nature of the electronic and atomic relaxation processes underlying the non-exponential change in measured conductivity [46, 47]. However, a large amount of literature dealing with PPC in III-Nitrides has been

---

[11] The time constants τ_{growth} and τ_{decay} describe the corresponding change in signal as either an increase to $(1 - 1/e) \approx 64\,\%$ or a decrease to $1/e \approx 37\,\%$ of the maximum signal.

published so far, and many different models have been proposed to explain the origin of PPC. An example transient build-up and decay curve of photocurrent in a GaN MSM photodetector sample is shown in Fig. 9.4. It can be seen that the photocurrent steadily increases during illumination at a constant optical power. After removing the light source, several processes are visible during the decay transient. The multi-exponential function (parameters given in the inset table) reproduces this switch-off behavior very well. However, there have been theoretical and experimental investigations considering macroscopic potential barriers at surfaces, interfaces, grain boundaries, and doping or material inhomogeneities that hinder the recombination process, in order to explain the long-decay constants $\tau \sim 10^3$ s in conjunction with the huge photoconductive gains $\sim 10^3$ observed in GaN photoconductors [49]. But most of the research reported refers to processes on the microscopic level, i.e., the trapping of free carriers at localized defects. Park et al. proposed that PPC in p-type GaN:Mg arises from the bi-stability of a nitrogen vacancy V_N accompanied by a change in the charge state [50]. Ursaki et al. reported for n-type GaN:Si that their measurements of photoconductivity reveal a mechanism associated with a broad distribution of electron traps located 2.2 eV below the conduction band [51]. They also concluded that rather the gallium vacancy V_{Ga} or the nitrogen antisite N_{Ga} may be the possible cause of PPC. Katz et al. proposed a model for PPC in n-GaN-based Schottky barrier PDs that considers the electron re-occupation of the filled hole traps at the semiconductor–metal interface after switching off the illumination, which then leads to a gradual recovery of the Schottky barrier [52].

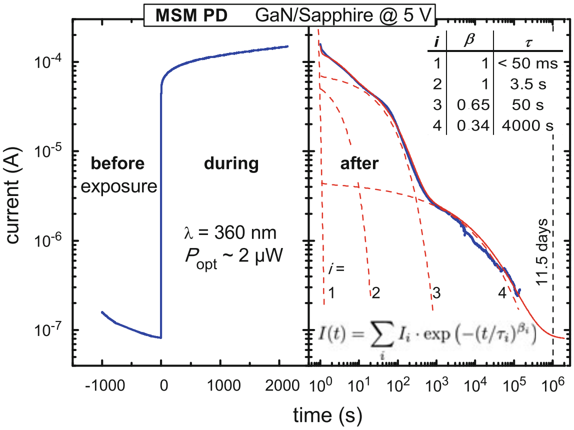

Fig. 9.4 Transient build-up (*left*) and decay curve (*right*) of photocurrent in a GaN MSM PD at 5 V bias upon 360 nm illumination. The decay transient can be modeled with a sum of stretched exponential functions; table lists the relevant parameters used for each contribution (unpublished data [48])

However, although the controversy about the origin of the PPC has not come to an end yet, many AlGaN-based photodetecting devices have been reported that do not show this unwanted effect. A deeper discussion of PPC is beyond the scope of this chapter and the reader is referred to the cited work and references therein.

9.2.1.5 Linearity

The linearity between I_{photo} and P_{opt} of a photoconducting device plays an important role, not only to define a power-independent responsivity Rsp as described in (9.8), but also to achieve reliable device operation. As mentioned for the rise and fall times, also the linearity is affected by the carrier recombination kinetics in the absorber material and the equivalent electrical circuit of the photodetector as well as the readout circuit.

Considering trap-free semiconductor material with a dark carrier density n_0 and an enhancement in carrier density Δn upon illumination at an optical generation rate G_{opt} ($\sim P_{\mathrm{opt}}$), the mono-molecular recombination via a single center may be investigated simply by arguing with rate equations for steady-state conditions [29]. For the insulator case ($n_0 \ll \Delta n$), it is found that a square root dependence $\Delta n \sim \sqrt{G_{\mathrm{opt}}}$ holds, whereas for the semiconductor case ($n_0 \gg \Delta n$), a linear dependence $\Delta n \sim G_{\mathrm{opt}}$ is valid. Including trapping centers, the situation becomes more complicated, but it can be summarized to depend on the energetic distribution of trap states. First of all, a uniform distribution of the density of traps, e.g., below the conduction band, can change the root dependence for the insulator into a linear relation. But also an exponential distribution of traps in the insulator case can change the power of G_{opt} from 1/2 to 1, when the incident power allows the light-induced free–carrier density Δn to stay below the density of trapped carriers ΔN_{t}. When for high intensity Δn becomes higher than ΔN_{t}, bimolecular recombination may dominate and thus $\Delta n \sim \sqrt{G_{\mathrm{opt}}}$ will be possible—even with trapping. Any trap-related non-linearities may change certain device properties in an uncontrollable way and thus are to be avoided.

Even if the material itself responds linearly to an incident photon flux, the connection to an external circuit causes limitations in the low and high power regimes. At the low end, the noise-equivalent-power, introduced further below, limits the photocurrent signal of any type of device. The saturation of photocurrent, e.g., in a p-i-n PD, at high power levels sets in above a value of about [53]

$$P_{\mathrm{opt,sat}} = \frac{q\phi_{\mathrm{bi}} - U_{\mathrm{bias}}}{(R_{\mathrm{S}} + R_{\mathrm{L}}) \cdot Rsp(\lambda)}, \tag{9.15}$$

where $q\phi_{\mathrm{bi}}$ is the built-in voltage drop across the p-i-n junction at zero bias and U_{bias} is the applied bias. Hence, this upper limit can be enhanced by applying a higher reverse bias ($U_{\mathrm{bias}} < 0$) or utilizing a smaller load resistance. Note also the dependence on the responsivity.

9.2.1.6 Detection Capability

The minimum detectable optical power of a photodetector is limited by different sources of noise. Noise arises either from certain detector properties and the readout setup, e.g., the noise in an amplifying transistor, or from the statistical fluctuations of the radiation signal and any significant background radiation during the detection process. For detailed description of noise sources, the reader is referred to the literature [31, 32, 54]. A very useful measure to compare the radiation-induced signal to the total noise of a detection system is the signal-to-noise ratio *S/N*. When the noise level in a detection system has been experimentally determined, the minimum detectable power, the noise-equivalent-power (NEP), can be estimated from $S/N = 1$. To compare the performance of different detection systems, the specific detectivity $D^* = \sqrt{AB}/\mathrm{NEP}$, with the detector area A and the bandwidth B, is commonly used. It is clear that the expressions for noise sources and consequently for D^* depend not only on the detector type and its design but also on the readout circuit components used. Thus, when designing the detector and readout for applications relying on high speed and precision, any noise from the electronic circuitry must be reduced below the detector noise level.

9.2.2 Various Types of Semiconductor Photodetectors

In this chapter, the principles of design and operation of the most common types of semiconductor photodetectors will be summarized. This includes the photoconductor, Schottky barrier photodiode (Schottky PD), metal–semiconductor–metal photodetector (MSM PD), p-i-n PD, and the avalanche photodiode (APD). Due to increasing interest in the development of wide bandgap semiconductor cathodes for efficient electron emitters also the phototube (PT) as well as the photomultiplier tube (PMT) and related issues will also be introduced.

9.2.2.1 Photoconductor

A photoconductive detector, also termed photoconductor, usually consists of a pair of ohmic electrodes processed on the semiconductor surface (see Fig. 9.5a). A large detection area can be realized utilizing an inter-digital arrangement of multiple pairs of electrodes. But this planar design also leads to a loss of optical signal due to the shadowing effect of electrodes. The current in the device is driven by the electric field between a pair of electrodes, which is adjusted by an externally applied bias U_{bias}. In the dark, i.e., when no radiation is absorbed, the dark current I_{dark} is given by $I_{\mathrm{dark}} = U_{\mathrm{bias}}/R_{\mathrm{dark}}$ with R_{dark} the resistance given by the dark resistivity of the material (dashed line in Fig. 9.5b). When the biased photoconductor is illuminated with photons having sufficient photon energy to create free carriers, i.e., $E_{\mathrm{opt}} \geq E_{\mathrm{gap}}$, the resistivity

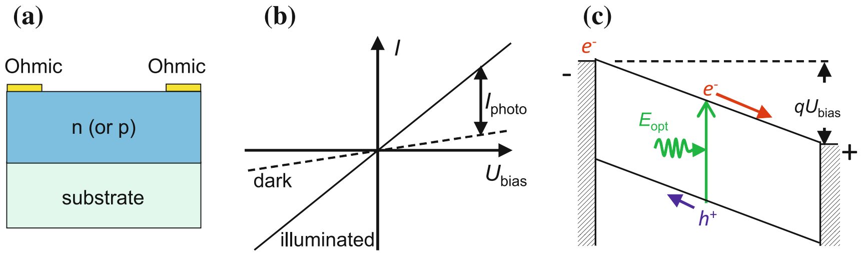

Fig. 9.5 **a** Cross-sectional schematic of a photoconductor. **b** Schematic I–V characteristics of a photoconductor in the dark (*dashed*) and under illumination (*solid*) (after [34]). **c** Schematic band diagram of the photoconductor biased under illumination

decreases to a value $R_{\text{illum}} < R_{\text{dark}}$. The photocurrent is then $I_{\text{photo}} = U_{\text{bias}} \cdot (R_{\text{illum}}^{-1} - R_{\text{dark}}^{-1})$ (full line in Fig. 9.5b). When a photoconductor, working in series on a load resistance R_{load}, is homogeneously illuminated with photons of optical power P_{opt} between its electrodes, at $R_{\text{load}} = 0$ the short-circuit photocurrent $I_{\text{photo}}^{\text{sc}}$ is given by [31]:

$$I_{\text{photo}}^{\text{sc}} = \frac{qP_{\text{opt}}}{E_{\text{opt}}} \cdot \eta_{\text{ext}} \cdot g \tag{9.16}$$

with the elementary charge q, the external quantum efficiency η_{ext}, and the gain factor g. Since electron and hole mobilities usually are different, e.g., $\mu_e > \mu_h$ in n-type material, the gain factor can be written as:

$$g = \frac{\tau_{\text{rec,h}}}{t_{\text{tr,e}}}, \tag{9.17}$$

where $\tau_{\text{rec,h}}$ is the hole recombination lifetime and $t_{\text{tr,e}}$ the electron transit time. Thus, in photoconductors a photoconductive gain mechanism occurs for certain values of $\tau_{\text{rec,h}}$ and $t_{\text{tr,e}} = d^2/\mu_{\text{e}} U_{\text{bias}}$, since the latter depends on the electrode spacing d, the electron mobility μ_{e}, and on the bias voltage U_{bias}. In a simplified picture, as illustrated in Fig. 9.5c, the photo-excited electron will reach the anode earlier than the hole—indicated by the different arrow lengths—and due to the requirement of charge neutrality an additional electron has to be injected at the cathode. This feedback lasts until a trapped hole captures a free electron. Thus, the number of electron loops increases g. It should be emphasized, that this gain does not refer to multiple carriers being generated by the absorption process of a single photon, but rather to the number of loops the faster sort of carriers can traverse the semiconductor before recombining with the slower (or trapped) carriers.

When scaling a photoconductor for an application, the limitations to the photocurrent due to electric field effects, such as space charge limited current, avalanche and dielectric breakdown come into play. Furthermore, a trade-off between a high gain factor and a fast response has to be found, since the device becomes slow when τ_{rec} is long. The main drawback of a photoconductor is the neccessity of a non-zero bias operation because the dark current levels give rise to additional noise and thus decrease the detectivity of the device. However, when a metal is available to form electrodes with ohmic behavior on the semiconductor, the fabrication of photoconductor devices is rather simple, compared to devices with several epitaxial layers, e.g., the p-i-n PD or an APD.

9.2.2.2 Schottky Barrier Photodiode

The Schottky barrier photodiode is based on the Schottky-type metal-semiconductor junction with rectifying current–voltage characteristics. As shown in Fig. 9.6a, a metal is deposited onto the optically active semiconductor layer that can be n- or p-type or even undoped. Prior to the moderately doped n-type (or p-type) absorber layer, a highly doped n^+-layer (or p^+-layer) is grown to reduce the contact resistance at the ohmic contact. In the following, a brief description of the n-type Schottky barrier diode and its characteristics will be given. For a deeper study on metal–semiconductor contacts, we refer the reader to the detailed monograph of Rhoderick and Williams [55] as well as to a recently published review on the physics and chemistry of the Schottky barrier by Tung [56]. The left image in Fig. 9.6b illustrates that for a Schottky barrier contact to be formed, the relation between metal work function ϕ_m, which is measured from the Fermi level $E_{F,\mathrm{m}}$ to the vacuum level E_vac, and the semiconductor electron affinity χ_s, which measured from the conduction band minimum E_C to the vacuum level, is essential. Within the concept of the Schottky-Mott theory, an ideal Schottky barrier of height $\phi_\mathrm{b} = \phi_m - \chi_s$ will be present for electrons facing the junction from the metal side if $\chi_s < \phi_m$. Below the metal electrode, a space charge region (SCR) is formed, being depleted of free electrons. This leads to an increasing electric field toward the

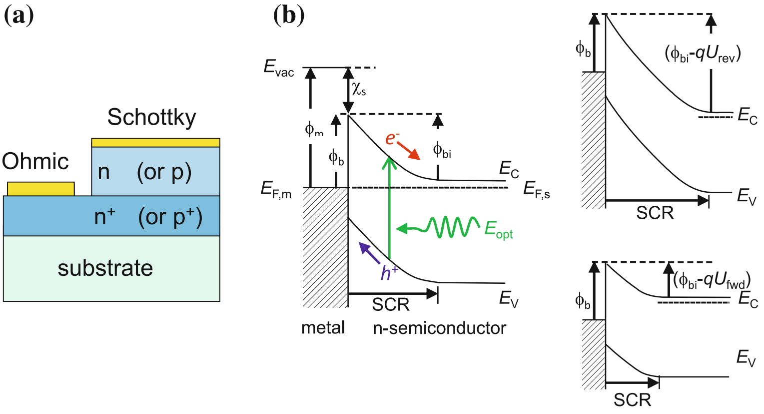

Fig. 9.6 **a** Cross-sectional schematic of a Schottky PD. **b** Band diagram of the metal/n-semiconductor junction under illumination at zero bias (*left*), and in the dark reversely biased $U_\mathrm{rev} < 0$ V (*right top*) as well as at forward bias $U_\mathrm{fwd} > 0$ V (*right bottom*)

metal–semiconductor junction due to an approximately constant density of positively charged ionized donors. This electric field causes an upward bending of the energy bands toward the surface, such that free electrons in the semiconductor have to overcome the built-in potential ϕ_{bi} to reach the metal contact. Biasing the Schottky contact negatively, as depicted in the top right image of Fig. 9.6b, enhances the potential barrier according to $\phi_{\mathrm{bi}} - qU_{\mathrm{rev}}$, with q the elementary charge and $U_{\mathrm{rev}} < 0$ V the reverse bias. The resulting net thermionic electron emission from the metal can be expressed as the saturation current density [55]

$$J_0 = A^{**}T^2 \exp\{-(\phi_{\mathrm{b}} - \Delta\phi_{\mathrm{b}})/kT\} \tag{9.18}$$

with Boltzmann's constant k, Richardson's constant A^{**}, the absolute temperature T, and the bias-dependent lowering $\Delta\phi_{\mathrm{b}}(U)$ of the Schottky barrier height due to image forces and dipole interactions at the metal/semiconductor interface. At very high-reverse bias conditions, band-to-band Zener tunneling or avalanche effects enhance the free-carrier density very rapidly resulting in the dielectric breakdown. Contrary, the bottom right image of Fig. 9.6b illustrates a barrier reduction due to forward bias conditions ($U_{\mathrm{fwd}} > 0$ V). This leads to an enhanced injection of electrons into the metal,[12] causing the current to increase exponentially. Thus, the current density of an ideal Schottky diode in the dark obeys a diode characteristics of the form [55]

$$J_{\mathrm{dark}} = J_0\{\exp(qU/kT) - 1\} \tag{9.19}$$

with J_0 given by (9.18). This relationship is further altered due to trap-assisted or phonon-assisted tunneling processes through the Schottky barrier, i.e., thermionic field emission or even field emission, all increasing with electric field strength close to the junction and thus with reverse bias U_{rev}. Further, shallow as well as deep energy levels, which can be induced by defects and impurities, may affect the charge distribution across the SCR and thus lead to a modification of the dark current characteristics discussed so far (see e.g., [57]).

For a Schottky diode operating as a radiation detector, the bias-dependent modulation of the depletion region characteristics, i.e., width and electric field distribution, is essential since photogenerated carriers in the SCR are separated and swept out by the electric field to contribute a drift current. Excess minority carriers in the field-free contact layer contribute a diffusion current, if generated within a diffusion length from the SCR. Thus, on the one hand, the resulting photocurrent signal I_{photo} depends on carrier transport mechanisms, such as the transit time of excess carriers and the minority carrier diffusion length. On the other hand, the incident photon flux, absorption coefficient, and minority carrier lifetime determine photogeneration and recombination processes. The *I–V* characteristics of a Schottky PD is very similar to that of other photodiode structures and for brevity, we refer to that depicted for the p-i-n PD shown in Fig. 9.8b. Accordingly, an

---

[12] Electrons are delivered by the ohmic contact.

unbiased Schottky PD already induces a short-circuit current upon illumination. This makes the Schottky PD an attractive alternative to the photoconductor that requires an external voltage.

Considering the design of a Schottky PD for front illumination, semitransparent metal layers have to be deposited for optimal photogeneration within the SCR near the Schottky junction, where the field is the highest. Furthermore, to minimize optical reflection losses, the top metal layer has to be very thin (<10 nm) and additionally an antireflection coating, optimized to a certain wavelength range, can be used.

9.2.2.3 Metal–Semiconductor–Metal Photodetector

A metal–semiconductor–metal (MSM) photodetector consists of two Schottky barrier junctions connected "back-to-back," as depicted in Fig. 9.7a. It means, separated metal electrodes are placed in the planar inter-digital arrangement side-by-side, on the surface of an optically active semiconductor absorber layer. As the device operation relies on the variation of the SCR regions near the metal electrodes, as in a Schottky PD, we distinguish the MSM PD from the photoconductor, which has two ohmic contacts and—ideally—no depletion region to separate photogenerated charges.

Due to the Schottky barrier contacts, the dark current flow is governed by either thermionic emission, thermionic field-emission or field-emission from the metal into the semiconductor and the barrier-lowering effects, as mentioned above for the Schottky PD [55]. But for the MSM device saturation currents for both, electrons at the cathode and holes at the anode, have to be considered [58]. Bias of any polarity reverses one electrode and forwards the other (see Fig. 9.7b) resulting in symmetric *I*–*V* characteristics in the dark as well as under illumination conditions (see Fig. 9.7c). By utilizing analytic expressions for the photocurrent in a simplified 1D-Structure, Sarto et al. found that recombination of photo-excited carriers almost

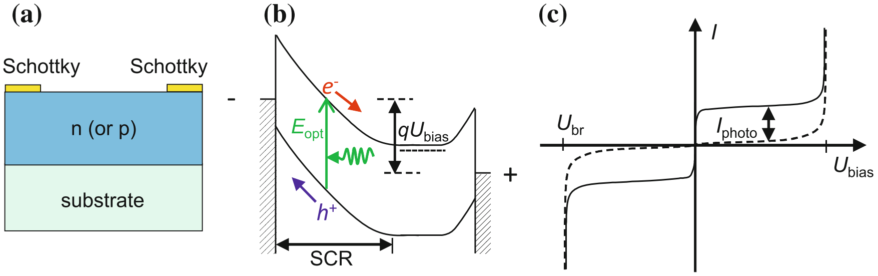

Fig. 9.7 **a** Cross-sectional schematic of an MSM photodetector. **b** Schematic band diagram of the MSM biased under illumination. **c** Schematic *I*–*V* characterisitcs of an MSM PD in the dark (*dashed*) and under illumination (*solid*)

has no effect on the dc characteristics and pulse response of a fully depleted absorber layer [59].

Due to the lack of a photovoltaic mode for an MSM, additional noise due to the bias applied has to be considered. However, the small contact area reduces the device capacitance leading to short *RC* time constants. Utilizing electrode spacings of several 10 nm enables for high-speed operation even in the THz range [60, 61].

9.2.2.4 p-i-n Photodiode

The p-i-n photodiode consists of an n-type layer, an undoped i-layer (i = intrinsic), and a p-type layer. As shown in Fig. 9.8a, additional p^+ and n^+ layers are used to form proper ohmic contacts with low contact resistances. In contrast to a pn-junction, the depletion region of a p-i-n diode is given by the i-layer and can be chosen to be much wider in order to allow for more efficient absorption as well as offering a lower junction capacitance, which is useful for high-frequency operation. Due to an almost constant electric field within the i-layer, the width of the SCR is nearly independent of the applied bias voltage resulting in a stable operation as well as increased breakdown voltage U_{br}.

Neglecting generation and recombination in the neutral i-region, the dark current of a p-i-n diode shows a diode behavior similar to (9.19), but with the saturation current density J_0 determined by minority carrier diffusion terms [34]

$$J_0 = q n_i^2 \left(\frac{D_p}{L_p N_{\mathrm{D}}} + \frac{D_n}{L_n N_{\mathrm{A}}} \right). \tag{9.20}$$

Here D_j with $j = n$ for electrons and $j = p$ for holes are the diffusion constants as well as $L_j = \sqrt{D_j \tau_{\mathrm{rec},j}}$ the diffusion lengths of the respective minority carriers, with the carrier lifetime $\tau_{\mathrm{rec},j}$. Further, n_i is the intrinsic carrier concentration, and N_{D} and N_{A} are the donor and acceptor concentrations, respectively. The dashed line in Fig. 9.8b illustrates the dark current characteristics of a p-i-n diode. At high-forward

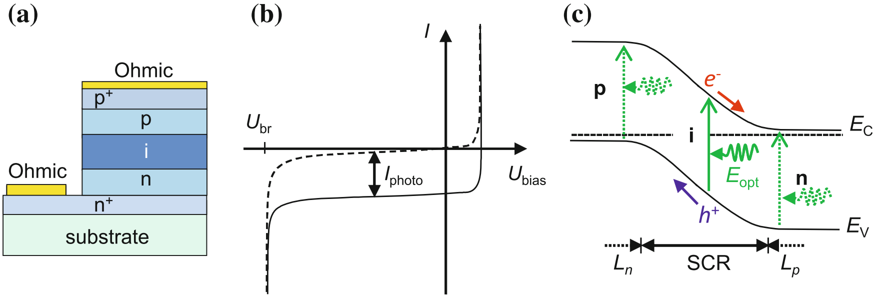

Fig. 9.8 **a** Cross-sectional schematic of a p-i-n PD. **b** Current–voltage characteristics of the p-i-n photodiode. **c** Band diagram of the p-i-n junction under illumination at zero bias

bias, the current will be limited due to the series resistance (not shown in the image) and at large reverse bias the breakdown due to avalanche effects and band-to-band Zener tunneling occurs. As illustrated in Fig. 9.8c, photogenerated excess charge carriers within the i-layer are swept out by the electric field even at zero bias and contribute a drift current, which is slightly enhanced by applying a reverse bias. Minority carriers being photogenerated within their respective diffusion length L_j from the depletion region are also swept across the field region and thus make up a current related to diffusion. The total photocurrent adds to the dark current as depicted by the solid line in Fig. 9.8b. However, depending on the illumination scenario (front or back), special care has to be taken in order to avoid absorption losses of the incident signal in these field-free layers before entering the absorber layer. Such absorption losses may be reduced and the diffusion tail in the temporal current signal can be suppressed, e.g., using very thin p- or n-type layers. Also appropriate heterojunctions can be used to reduce the diffusion tail: when choosing a wider bandgap for the doped entrance layer in comparison to the absorbing i-layer, the radiation within a certain spectral range can reach the i-layer. However, this approach is challenging in terms of fabrication, regarding the issues with doping and ohmic contact formation in the III-Nitrides, as will be discussed further below.

9.2.2.5 Avalanche Photodiode

An avalanche photodiode (APD) can be designed in several ways, since its operation principle is based on a carrier multiplication mechanism by impact ionization processes at high electric fields near breakdown. Regions of high electric field are generally the depletion regions that have different field distribution depending on the device structure and are present below and especially near the edges of a Schottky-type contact (MSM and Schottky PD) and at the p-n junction or within the i-layer of the p-i-n PD at a sufficient reverse bias. When a free-carrier gains sufficient kinetic energy ($> E_{\mathrm{gap}}$), i.e., negligible energy loss due to collisions with the lattice occuring during its travel, the excitation of additional e–h pairs can be initiated—(1), (2), (1′), and (2′) in Fig. 9.9a—and these impact ionization processes consequently lead to carrier multiplication. In general, the probabilities of impact ionization are different for electrons and holes and are described per unit length (cm^{-1}) via the respective ionization coefficients α_n and α_p, which have a dependence on the electric field strength F as [31]:

$$\alpha_i = \alpha_{i,0} \cdot \exp(-F_i/F)^{\gamma}, \tag{9.21}$$

where $i = n,p$ for electrons and holes, and γ, $\alpha_{i,0}$ as well as F_i are the fitting parameters to experimental results or calculations. The inset in Fig. 9.9b shows impact ionization coefficients as a function of the inverse electric field as calculated by Oguzman et al., for electrons (black squares) and holes (red squares) in wurtzite phase GaN [62] and fits to these data with (9.21) for $\gamma = 1$ (full lines). According to these results, the ionization coefficient for holes is larger than for electrons in GaN

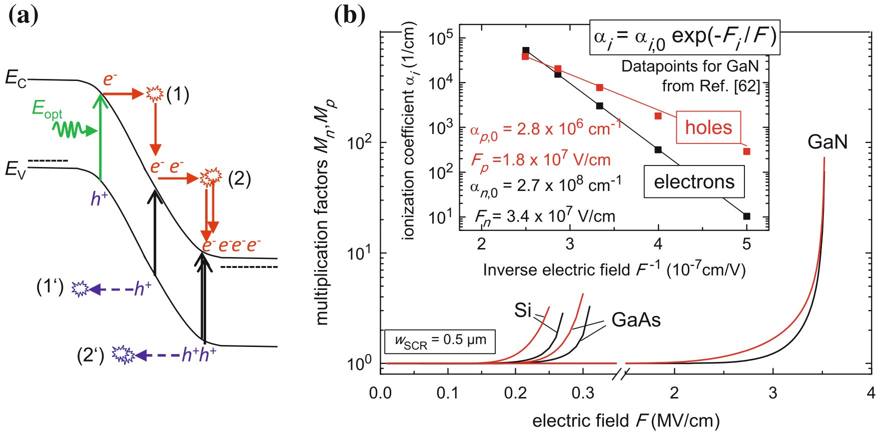

Fig. 9.9 **a** Schematic of carrier multiplication in a highly reverse-biased p-i-n structure: Impact ionization occurs upon electron injection at the p-side. **b** Multiplication factors calculated after (9.22) for pure electron (*black*) or hole (*red*) injection into the multiplication region of a reverse-biased p^+-π-n^+ photodiode based on either Si, GaAs or GaN; the inset shows data (from [62]) for electron and hole ionization coefficients in GaN with a fit of (9.21) (further explanation in text)

for electric fields below 3.7 MV cm^{-1}, indicating hole-initiated avalanche processes to occur at a higher rate. Thus, while the p-i-n *I–V* characteristics at low fields are as described above for the other PD types, at high fields the carrier multiplication due to impact ionization increases the current in the device by the multiplication factor M_i. These multiplication factors can be derived for any particular PD type. In a p^+-π-n^+ diode (π = very low p-type) with constant electric field in the π-region of width w the multiplication factors can be written as [31]:

$$M_i = \frac{(1-k_i)\cdot \exp[\alpha_i \cdot w \cdot (1-k_i)]}{1-k_i \cdot \exp[\alpha_i \cdot w \cdot (1-k_i)]} \quad (i = n, p), \tag{9.22}$$

where $k_n := \alpha_p/\alpha_n$ is the ionization ratio, and $k_p = 1/k_n$. Multiplication factors calculated with (9.22) for electron (black) and hole (red) multiplication in Si, GaAs, and GaN are shown in Fig. 9.9b for an i-layer thicknesses of $w_{\mathrm{SCR}} = 0.5$, where α_i values for Si and GaAs have been calculated after [31] and those for GaN are shown in the inset of Fig. 9.9b. Thus, for GaN the multiplication of carriers is expected to set in at electric fields an order of magnitude higher, than for Si and GaAs. However, since α_i as well as the k_i are exponential functions of the inverse electric field, small changes in F cause a very steep increase in M_i near the breakdown field for $k_n > 1$. In this case, the stable operation of such a p^+-π-n^+ diode becomes critical, whenever electrons and holes are injected simultaneously in the same high-field region. Due to spatial inhomogeneities in either the doping profile or the width w_{SCR} of the space charge region the electric field strength varies locally, so that, if $\alpha_n < \alpha_p$ holds, a sudden multiplication of electrons can deteriorate the device performance or even cause local breakdown effects.

Thus, it is preferred to separate the absorption region, an i-layer for electron and hole photogeneration, from the multiplication region, another i-layer, where ideally one type of carriers is injected to initiate multiplication. The resulting separate absorption and multiplication (SAM) APD structures are manifold, e.g., the p^+-n-ν-n^+ (ν = very low n-type) or p^+-n^--n-ν-n^+ (lo-hi-lo) structure, and thus, the target spectral range, the temporal behavior as well as the prevailing carrier type for impact ionization have to be considered for their design. Experimentally, the multiplication factor for the photocurrent signal at a fixed bias can be deduced using [31]

$$M_{\text{photo}} = \frac{I_{\text{M,photo}} - I_{\text{M,dark}}}{I_{\text{pr,photo}} - I_{\text{pr,dark}}}, \tag{9.23}$$

where I_{M} and I_{pr} are the multiplied and the primary (unmultiplied) current signals, respectively. For the detection of modulated radiation, the limitations to device performance due to a constant product of multiplication factor M and bandwidth $f_{\text{c}-\text{o}}$ as well as the influence of noise, measured by the effective excess noise factor, have to be considered for optimal operation (see e.g., [31, 63]). Finally, it should be noted, that the breakdown voltage due to avalanche processes increases for increasing temperature (positive temperature coefficient), since the lattice vibrations cool down the hot carriers. Zener-tunneling causes opposite behavior (negative temperature coefficient), since the bound carriers gain energy to overcome the tunneling barrier at a smaller voltage. Therefore, these processes can be distinguished by their temperature dependence.

9.2.2.6 Phototube and Photomultiplier Tube

The phototube is a gas filled or vacuum tube containing an element being sensitive to radiation due to the external photoelectric effect. Such a tube consists of two opposite electrodes, cathode and anode, in a sealed glass tube. The cathode, located at an entrance window either in transmissive or reflective mode, is coated with a photo-emissive material sensitive to a desired wavelength range. Photons entering the entrance window hit the photocathode material and excite electrons that may be released from the cathode surface, if the excess kinetic energy delivered by the

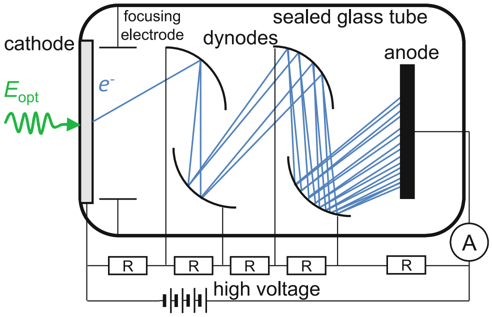

Fig. 9.10 Cross-sectional schematic of a photomultiplier tube (PMT)

photons is sufficiently large, as will be discussed below. The electrons freed at the cathode are then accelerated toward the positively biased anode and cause an electric current of a few microamperes in an external circuit. A photomultiplier tube (PMT) is a modification of the vacuum phototube, where the primary photocurrent emitted from the cathode is multiplied at subsequent electrodes, the dynode stages as shown in Fig. 9.10. When every dynode is held at a more positive potential compared to its prior electrode, electrons in the vacuum gain a corresponding kinetic energy. Depending on the dynode material, the applied voltage has to be chosen accordingly, to create secondary electrons at every stage. Thus, an electron emitted at the cathode hits the first dynode stage and generates secondary electrons that are accelerated toward the second dynode, and so on, until an increased number of electrons reaches the anode and causes a current signal that is proportional to the amount of incident photons. The multiplied current produced by incident radiation can be enhanced by factors of up to 10^7 depending on the number of dynode stages. This enables a PMT for applications where single photons have to be detected.

A PMT can be designed, like the simple phototube, by choosing the suitable photo-emissive cathode material to meet different wavelength ranges in the UV, the visible, and the NIR spectral regions. Due to its high sensitivity, a PMT has to be protected from radiation that may irreversibly harm the dynode coating due to excessive current levels. As for any photodetector type, the transmission of the window material limits the spectral bandwidth and height of the device responsivity. The physical processes occuring in the cathode material upon illumination can be understood utilizing the simple three-step model of photoemission which was developed by Spicer and Berglund for alkali-antimonides [65–67]. As illustrated in Fig. 9.11a, these steps—(1) optical excitation, (2) electron transport in the p-type solid and (3) carrier escape accross the surface—can be treated separately [64]. The electron emission efficiency η_e of a photocathode is approximated by

$$\eta_e = (1 - R_{opt}) \frac{\alpha^\dagger}{\alpha} \left\{ \frac{P_e}{1 + 1/\alpha L_n} \right\} \tag{9.24}$$

with R_{opt} the optical reflection, α the optical absorption coefficient, $\alpha^\dagger$ the absorption coefficient for excitation into states above the vacuum level, P_e the probability of electron escape into the vacuum, and L_n the electron diffusion length in p-type material. Neglecting band bending effects due to Fermi level pinning, which is caused by a high density of defect levels at the surface, from (9.24) it is clear that the spectral shape of η_e is governed by a threshold energy $E_{thr} = E_{gap} + \chi$, where χ is the electron affinity of the material defined as the energy distance between the vacuum level and the bottom of the conduction band right at the surface (c.f. Fig. 9.10a). Since a modification of electronic surface properties by adsorbate-induced surface dipoles and surface states—e.g., due to the formation of a Cs, Cs_2O, Li or NF_3 adlayer with rather n-type properties on the surface of p-GaAs [68, 69]—can result in a band bending at the surface below the conduction band minimum in the bulk material, it is possible to obtain a negative electron

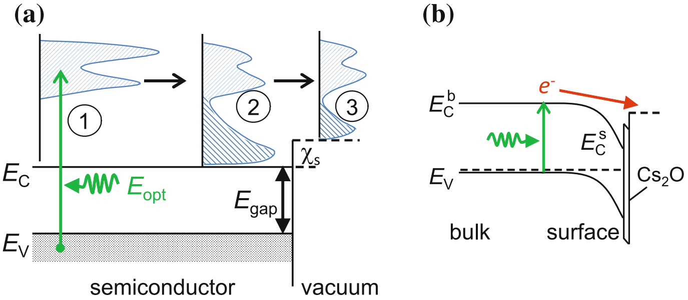

Fig. 9.11 **a** Schematic band diagram of semiconductor/vacuum junction showing three steps of photoemission of electrons: *1* excitation, *2* transport, and *3* escape (after [64]). **b** Schematic band diagram for effective negative electron affinity (NEA) assisted by Cs_2O adlayer on the p-type semiconductors surface

affinity (NEA), as shown in Fig. 9.11b. The semiconductor NEA may be *effective*, corresponding to E_{vac} below the bulk conduction band minimum E_C^b, or *true*, when E_{vac} is below the surface conduction band minimum E_C^s. For effective NEA, the affinity χ is positive but small and the energy bands are bent downward at the surface, as it may occur for a p-type semiconductor. If electrons, excited in the bulk, thermalize to E_C^b and further travel ballistically across the depletion region toward the surface, they have sufficient kinetic energy to escape from the semiconductor. In the case of true NEA, electrons thermalized even at the surface have sufficient energy to escape from the solid. Consequently, in NEA semiconductors the cathode threshold energy for electron emission is reduced and an enhancement of η_e is achievable. This makes such materials attractive for efficient electron emitters for the use in phototubes or PMTs.

9.3 III-Nitrides for Solid-State UV Photodetection

The ability to directly tune the detector cut-off wavelength via the Al mole fraction x_{Al} of the active layer is one of the main advantages of the $Al_xGa_{1-x}N$ material system compared to e.g., SiC, diamond or other elemental materials. This enables the blocking of unwanted signals with wavelengths above 365–200 nm, depending on x_{Al}, and thus the exploration of the UV-A, UV-B, and the UV-C spectral region without the use of additional filters. A comparison of typical responsivity spectra of Schottky (GaP, GaN, AlGaN) as well as p-i-n (SiC) photodiodes is shown in Fig. 9.12 (unpublished data [70]). The GaP photodiode EPD-150 covers a wide range of wavelengths from 150 nm up to the VIS spectral range with EQE levels between about 8 % at 150 nm and 30 % at 410 nm. In combination with an external low-pass filter for a cut-off at 365 nm, the spectrum of the photodiode EPD-365 (GaP + Filter) shows cut-offs in the UV-C at about 260 nm and in the UV-A

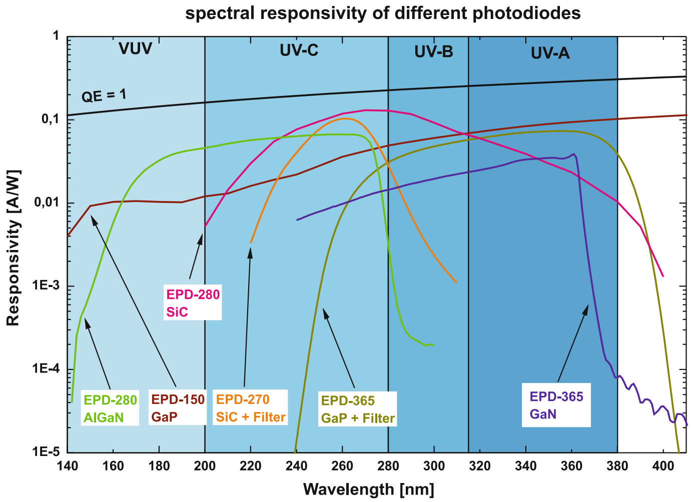

Fig. 9.12 Comparison of responsivity spectra for different types of photodetectors (unpublished data [70])

at about 380 nm. But due to the high-absorption values for GaP for $\lambda \geq 360$ nm (c.f. Fig. 9.1b), the UV-A cut-off results in a rather weak rejection of signals up to 400 nm: The responsivity of 70 mA W^{-1} at 380 nm corresponds to a quite high EQE of about 22 %. A similar situation can be observed for a SiC photodiode. Due to its indirect bandgap, the EPD-280 (SiC) without external filter covers the range from 200 to 400 nm not showing a sharp cut-off but a peak responsivity of about 100 mA W^{-1} at 280 nm. An external filter for UV-C limits the detection range from 220 to 315 nm, as it is shown for the SiC EPD-270 (SiC + Filter). So it is possible to tune a photodetectors spectral range of responsivity using external filters but in conjunction with the optical properties of the semiconductor used, the spectral performance is often limited. However, the main drawbacks to be mentioned are the commercial availability, the price, and the degradation of the filter characteristics. Whenever precise requirements for a specific UV application rely on the filter characteristics, the $Al_xGa_{1-x}N$ material with its tunable intrinsic cut-off promises true visible-blind or solar-blind operation, as it is shown in Fig. 9.12 for the GaN photodiode EPD-365 as well as for the $Al_{0.45}Ga_{0.55}N$ photodiode EPD-280.

Despite the difficulties in AlGaN epitaxy and processing mentioned in the introduction, the first report on photoconductivity measurements in GaN samples was by Pankove and Berkeyheiser in 1974. In this early work, the near-gap photoconductivity edge was attributed to the fundamental absorption edge of GaN:Zn crystals grown by hydride vapor phase epitaxy (HVPE) [71]. The samples were prepared with soldered indium contacts in order to study the photoconductive properties of the material as a function of Zn doping. Where as-grown HVPE GaN films at those times were usually found intrinsically n-type due to very high concentrations of nitrogen vacancies [72], an abrupt transition of the electrical properties from conducting to insulating as well as an enhancement of material quality

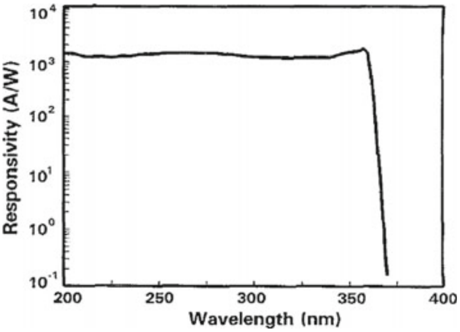

Fig. 9.13 Responsivity spectrum of the first MOCVD grown GaN-based photoconductor device at 5 V bias. Reprinted with permission from [73], Copyright 1992, AIP Publishing LLC

was observed as the Zn concentration was increased. From these findings, it was concluded that Zn atoms would occupy the vacant N sites, and thus reduce the dark conductivity.

About two decades later, in 1992, Khan et al. utilized a low pressure metal organic chemical vapor deposition (MOCVD)-based growth technique, called switched atomic layer epitaxy (SALE), in order to obtain insulating GaN films [3] and shortly after that they also showed characterisation results of the first UV photodetectors fabricated on such GaN layers grown on an AlN/sapphire template [73]. The GaN photoconductors processed had an inter-digital arrangement of Au-electrodes. The *I–V* characteristics of those sensors were linear with dark current level as low as 2 nA at 200 V. At 5 V applied bias, a rather flat responsivity spectrum of 1000 to 2000 A W^{-1} between 200 to 365 nm was obtained with an abrupt drop in signal by three orders of magnitude within 10 nm of the band edge (see Fig. 9.13). Despite the presence of a very high photocurrent gain of 6×10^3 at 365 nm, the response of those devices at 254 nm was found to be linear over five orders of incident optical power and the bandwidth was in excess of 2 kHz. In summary, those first results illustrated a very high potential of GaN material for UV sensing applications.

In the following, many other research groups also succeeded in developing AlGaN-based UV photosensitive devices such as photoconductors, phototransistors, MSM detectors, Schottky barrier photodiodes, MIS diodes as well as p-n and p-i-n diodes. Even the integration of AlGaN-based focal-plane arrays to silicon read-out circuits was achieved and thus the applicability of the III-Nitrides on a rather complex level of technology was demonstrated [74].

9.3.1 AlGaN-Based Photoconductor

First studies on AlGaN-based photoconductors indicated the potential of III-Nitrides, despite some findings that might also hamper device operation in several applications. The high photoconductive gain levels reported led to long-decay times in the ms range and thus device operation was usually limited to kHz-bandwidths. The gain mechanism was attributed to either the trapping of photogenerated holes and the resulting enhanced effective electron lifetime [75] or the light-induced modulation of the conductive volume [49, 76]. Furthermore, photoconductor devices require biasing, which leads to additional dark current noise. Thus, specific detectivities reported were as low as 10^7–10^9 cm $\mathrm{Hz}^{1/2}$ W^{-1} [73, 77]. With increasing Al content in the $\mathrm{Al}_x\mathrm{Ga}_{1-x}\mathrm{N}$ layers, the free carrier lifetime was found to decrease as the material becomes more insulating. This result was attributed to an exponential distribution of band-tail states due to the potential fluctuations which arise from an increasing density of defects [78]. Linear photocurrent-power dependencies, even over a wide range of power levels [79] as well as sublinear responses and excitation-dependent response times were observed [80]. Additionally, metastability and persistent photoconductivity (PPC) effects, which can lead to decay times in the order of several 1000 s, were observed in p-type [81] as well as n-type [82] material.

In conclusion, despite the high photocurrents achieved in GaN photoconductors, the gain-related issues, such as device bandwidth and linearity, restrict that type of PD to low frequency applications. In addition to that, the difficulties in processing proper ohmic contacts with increasing x_{Al} impede the development of AlGaN-based photoconductors for the UV-C range.

9.3.2 AlGaN-Based MSM Photodetector

Metal–semiconductor–metal (MSM) photodetectors based on AlGaN offer some advantages over other device types considering their simple fabrication process, since no p- or n-type doping is required and they are easy to integrate in planar process technology. But as well as the photoconductors, metal–semiconductor–metal PDs need an external bias to be driven. This complicates the evaluation of scientific reports, since there is no standard for the bias voltage at which an MSM PD needs is operated.

However, first GaN MSM PDs were demonstrated with an EQE of about 50 % at 6 V, 350 nm cut-off wavelength, a high rejection to visible-light, and low dark current of 800 fA at 10 V [83]. MSM PDs are capable of very high-speed operation, when fully depleted. GaN MSM devices, having 2 μm electrode spacing, with a rise time of 23 ps and a 3 dB cut-off frequency of 16 GHz have been shown [84]. An analysis of the MSM PD performance considering bias and electrode spacing indicates a transit time-limited operation and the modeling of the temporal response reveals the slower holes, compared to electrons in GaN, to be responsible for a slow tail measured experimentally (see Fig. 9.14). However, MSM PDs have been subject to a huge number of publications. In the year 2000, back-illuminated solar-blind $\mathrm{Al}_x\mathrm{Ga}_{1-x}\mathrm{N}$ MSM PDs with 260 nm peak wavelength have been presented [85]. As shown in [86], a significant overlap between the depletion region below the biased contacts on the front surface and the photon absorption depth at

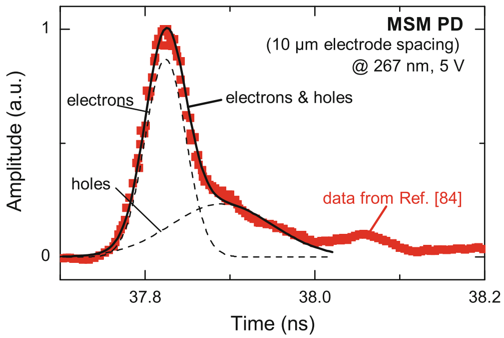

Fig. 9.14 Measured photo-response transients (*scatter*) of a GaN MSM PD with 10 electrode spacing upon pulsed excitation at 267 nm under 25 V. For the modeled data (*lines*) contributions of fast electrons and slow holes have been assumed (data taken from [84])

the backside of the device has to be created either by increasing the bias voltage or decreasing the absorber layer thickness sufficiently. For this reason, the EQE found in [85] increases from about 4.7 % at 4 V to about 48 % at 100 V. The dark current level in this device stayed below the experimental detection limit of 20 fA. Operation of solar-blind MSM PDs under 150 °C temperature has been demonstrated recently [87]. The Al$_{0.4}$Ga$_{0.6}$N MSM PD with semitransparent Ni/Au contact electrodes showed a low-dark current in the fA-range at elevated temperature up to 20 V bias and a breakdown voltage higher than 300 V. At 10 V bias, the peak EQE of about 64 % at 275 nm and room temperature and was decreased by only 20–40 % with increasing temperature, possibly due to enhanced carrier recombination losses at elevated temperatures. Pt-AlN MSM detectors with a very low dark current below 100 fA up to 200 V and a very sharp cut-off at 207 nm showed a peak responsivity of 0.4 A W^{-1} at 200 nm for 100 V bias. The reported data (EQE $\sim$ 2.4 at about 200 nm) indicate a bias-dependent gain. Nevertheless, these results demonstrate AlN MSMs as suitable candidates for DUV device applications [88].

Al$_{0.4}$Ga$_{0.6}$N layers grown on laterally overgrown AlN on stripe-patterned AlN/sapphire templates turned out to exhibit anisotropic compositional fluctuations throughout the epilayer [89]. At elevated bias, the solar-blind MSM PDs on this material operated linearly with incident optical power but with anisotropic characteristics. Devices with electrodes oriented perpendicular to the underlying stripe pattern showed photoconductive gain (EQE $\sim$ 77 at 30 V) which was absent in devices with parallel electrode orientation. An exponential quenching of this anisotropic EQE with temperature increased from room temperature to about 150 °C was observed and it was suggested that the gain has to be due to a carrier accumulation mechanism at the interfaces between the matrix material with high Al-content and the Ga-rich stripes with a smaller bandgap [90]. This allows not only for highly sensitive devices but also for different detector characteristics integrated on the same wafer.

In summary, a high detection capability achieved by the electrode geometry, the processing of Schottky-type electrodes as well as the epitaxy of non-intentionally doped $Al_xGa_{1-x}N$ layers within the whole composition range make the AlGaN-based MSM PD an easy-to-fabricate device. Moreover, by backside illumination of properly designed MSM PDs, the optical loss due to electrode shading can be circumvented.

9.3.3 AlGaN-Based Schottky Barrier Photodiode

The first AlGaN-based Schottky-type PD was a back-illuminated 1 mm^2 Ti/Au p-type GaN:Mg device with a zero bias EQE of 50 % at 320 nm ($Rsp \sim 0.13\,A.W^{-1}$) and a response time of 1 µs [91]. On n-type GaN material Schottky barrier heights of 0.88, 0.92, 0.99, and 1.08 eV were obtained for Au, Pd, Ni, and Pt, respectively [92]. A front-illuminated device consisting of a semi-transparent Pd layer on n-GaN was fabricated and characterized with $Rsp \sim 0.18\,A.W$ and a *RC*-limited decay time of 118 ps [93]. Dominant leakage current mechanisms through GaN—as well as AlGaN-Schottky interfaces were recently found to be well described by donor-like surface states which reduce the depletion width and enhance tunneling transport processes [94]. Photoconductive gain mechanisms were attributed to the trapping of minority carriers at the semiconductor/metal interface in conjunction with a subsequent reduction of the Schottky barrier height, such that electron tunneling processes through the barrier are enhanced [52]. UV-B photodetectors with an active $Al_{0.25}Ga_{0.75}N$ layer grown on an $Al_{0.2}Ga_{0.8}N$/GaN superlattice layer (SL) stack showed superior device performance compared to those PDs without SL [95]: Dark current as low as 100pA at −5 V, zero bias responsivity of 97 mA W^{-1} and specific detectivity of 8×10^{13} cm $Hz^{1/2}$ W^{-1} at 290 nm were reported. Solar-blind AlGaN Schottky photodetectors with a diameter of 800 have been fabricated [96]. These devices on AlN/sapphire templates consisted of a semitransparent Ni/Au contact on 200 nm undoped i-$Al_{0.5}Ga_{0.5}N$ deposited on a doped n-AlGaN layer contacted with Ti/Al ohmic contacts. These devices showed responsivity in the range between 100–265 nm under front illumination. High-quality AlN Schottky PDs on an n-type SiC substrate showed a cut-off at 210 nm and a zero bias peak responsivity of 0.12 A W^{-1} at 200 nm corresponding to an EQE of about 74 % (Fig. 9.15). The very low dark current levels of below 1 pA up to 150 V reverse bias as well as the zero bias detectivity of about 10^{15} cm $Hz^{1/2}$ W^{-1}, which is comparable to the detectivity of conventional PMTs, demonstrate the potential of AlN Schottky diodes for DUV optoelectronic device applications [97].

The AlGaN-based Schottky-type photodetectors developed so far show low dark currents due to the blocking Schottky contact, and despite the use of semitransparent metals, high values for the zero bias EQE could be achieved. In comparison

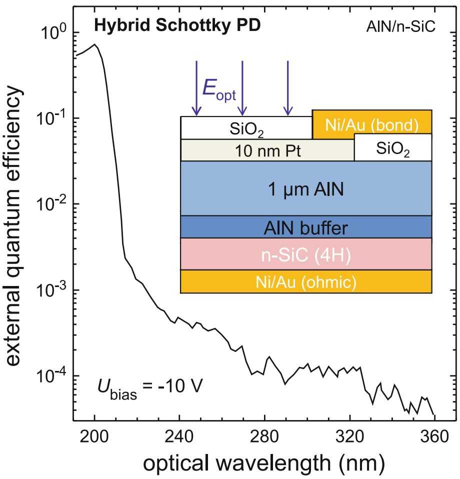

Fig. 9.15 External quantum efficiency of a hybrid Pt-AlN/4H-SiC Schottky PD biased at −10 V; the *inset* shows the device structure with SiO_2 passivation layers (EQE calculated from [97])

to the MSM PD, the difficulties of doping and ohmic contact formation with increasing x_{Al} remain an issue for that type of PD.

9.3.4 AlGaN-Based p-i-n Photodiode

The device structure of a visible-blind GaN based p-i-n photodiode usually consists of an n-type GaN:Si layer with a free-electron concentration of $n \sim 10^{19}$ cm^{-3} followed by an intrinsic GaN region with a background concentration of $n \sim 10^{16}$ cm^{-3} and a top p-type GaN:Mg layer with a hole concentration ranging between 10^{17} to 10^{18} cm^{-3} (see e.g., [98]). Additionally, highly doped n^+- and p^+-type layers are utilized to lower the contact resistance at the device terminals. After mesa-etching down to the n-layer region, proper ohmic contacts with low contact resistances need to be processed on both of the doped layers. An entrance area for the device can now be realized for front- or backside illumination. In both cases, optical losses due to reflection at interfaces as well as due to absorption need to be minimized. For front-illuminated PDs, meshed contacts on the p-layer can be used to reduce electrode shading losses [99]. GaN devices with a semitransparent p-$Al_{0.13}Ga_{0.87}N$ entrance window on top of the photoactive intrinsic GaN region have been reported [100]. An ohmic Ni/Au contact ring on an etched p^+-GaN cap layer defines the entrance window to the absorber layer, which was passivated by a SiO_2 layer. The EQE spectrum at 1 V is flat on a level of about 45 % in the band between 365 to 330 nm and then decreases toward short wavelength due to the onset of absorption in the p-AlGaN layer. For back-illuminated GaN p-i-n devices, an n-$Al_{0.28}Ga_{0.72}N$ layer/i-GaN heterojunction was used and a zero bias EQE of 75 % at 355 nm could be obtained [101]. To achieve solar-blind operation in back-illuminated devices, all layers below the active $Al_xGa_{1-x}N$ layer with

$x_{\mathrm{Al}} \geq 0.45$ have to be transparent for the incident radiation. Hence, either substrates opaque to UV-C radiation (Si, SiC) have to be removed or sapphire has to be used. Using this approach, the responsivity of a back-illuminated device is spectrally limited to a narrow wavelength band, which is defined by the different bandgap energies in the layer stack. Besides a sufficient optical transparency, the electronic properties of the n- and the n^+-$\mathrm{Al}_x\mathrm{Ga}_{1-x}\mathrm{N}$ layers have to be properly optimized in order to achieve low-series resistance, i.e., high mobility and electron concentration. At x_{Al} of about 60 % an electron mobility of 20 $\mathrm{cm}^2\ \mathrm{V}^{-1}\ \mathrm{s}^{-1}$ and electron concentration of $1 \times 10^{19}\ \mathrm{cm}^{-3}$ could be achieved at room temperature, which resulted in a zero bias EQE of 58 % at 274 nm for solar-blind p-i-n PDs [102]. The minimization of any voltage drop across the p- or the n-layers is necessary in order to confine the depletion region to the i-layer and also to enhance the carrier collection efficiency *CE* due to reduced minority carrier losses [103]. Record high zero bias EQE values of about 80 % at 275 nm have been reported recently for the back-illuminated solar-blind diodes (see Fig. 9.16) [104]. The high quality of a Si-In co-doped n^+-type $\mathrm{Al}_{0.5}\mathrm{Ga}_{0.5}\mathrm{N}$ window layer with resistivity, mobility, and carrier concentrations of $1.55 \times 10^{-2}\ \Omega$ cm, 74 $\mathrm{cm}^2\ \mathrm{V}^{-1}\ \mathrm{s}^{-1}$, and $4.41 \times 10^{18}\ \mathrm{cm}^{-3}$, respectively, is claimed to significantly contribute to these results.

Since specific detectivities in the range between 10^{13} and 10^{15} cm $\mathrm{Hz}^{1/2}\ \mathrm{W}^{-1}$ have been reported during the last two decades for p-i-n-type PDs [99, 105–107], it is an attractive alternative device to the PMT whenever low intensity signals have to be detected. Even flame luminescence detection between 250 to 280 nm in the nW cm^{-2} range was demonstrated under fluorescent room light with a front-illuminated n-$\mathrm{Al}_{0.44}\mathrm{Ga}_{0.56}\mathrm{N}$/i-$\mathrm{Al}_{0.44}\mathrm{Ga}_{0.56}\mathrm{N}$/p-GaN/p-mesh heterojunction photodiode [108].

Due to the heterojunctions in a p-i-n sample stack, the effects of piezoelectric polarization (in combination with the spontaneous polarization of the absorber layer) have to be considered. According to modeling results of Kuek et al., dealing

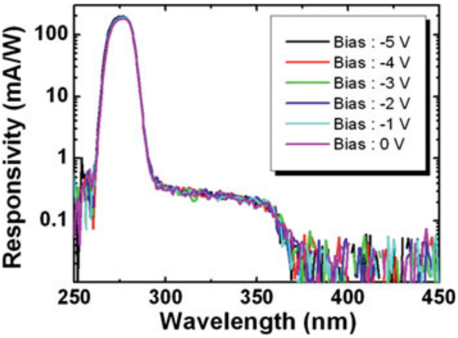

Fig. 9.16 Responsivity spectra of back-illuminated solar-blind p-i-n PDs biased up to −5 V, the maximum peak responsivity at −5 V of about 200 mA/W corresponds to 89 % external quantum efficiency. Reprinted with permission from [104], Copyright 2013, AIP Publishing LLC

with the effect of polarization charges in a UV-B p-GaN/i-$Al_{0.33}Ga_{0.67}N$/n-GaN PD [109], the polarization-induced interface charges increase the barrier to carriers photogenerated within the GaN regions resulting in an enhanced rejection of UV-A radiation.

The development of p-i-n PD profits from the advancing development of AlGaN-based emitting devices, such as LEDs and laser diodes, and vice versa. However, the uniformity of the high electric field and its confinement to the i-layer both play key roles concerning device stability and reliability. A broad range of the UV-region could be covered by the utilization of heterojunction devices as well as the backside illumination approach. The doping and contact formation issues are usually handled by utilizing a sophisticated layer structure including heterojunctions. Therefore, any progress in the fabrication of AlGaN-based p-i-n PDs supports the development of AlGaN-based avalanche photodetectors, discussed in the next paragraph.

9.3.5 AlGaN-Based Avalanche Photodetector

An avalanche photodiode (APD) is usually realized utilizing carrier multiplication in an optimized structure of the p-i-n diode type or the SAM photodiode introduced in Sect. 9.2. However, avalanche multiplication due to soft breakdown characteristics is also found for many of the conventional AlGaN-based devices. These results will be discussed first.

A visible-blind MSM structure with its planar rectifying electrodes is subject to enhanced electric fields within the semiconductor at the metal contact edges. A maximum field strength of 3.5 MV cm^{-1} at a bias of 134 V was estimated by simulating the electrical properties of such a device. These fields are high enough to initiate impact ionization, such that an avalanche gain of more than 1188 at 145 V was measured [110]. For a solar-blind p-i-n structure, a maximum optical gain of 700 at a reverse bias of 60 V was achieved without evidence of abrupt breakdown [111]. The electric field strength at the onset of impact ionization was estimated to be about 1.7 MV cm^{-1}. A solar-blind Schottky PD was reported with 1560 gain at 68 V and a detectivity as high as 1.4×10^{14} cm $Hz^{1/2}$ W^{-1}. For the Pt/AlN Schottky PD on an n-SiC substrate a gain as high as 1200 at 250 V reverse bias was obtained [112]. In all cases mentioned, the bias- and temperature-dependencies have been investigated in order to rule out Zener-tunneling or photoconductive gain as dominant mechanisms for the breakdown process.

Homoepitaxial GaN APDs, illuminated from the top-side, have been reported by Dupuis et al. [113]. As shown in Fig. 9.17, an almost constant and low-leakage current level of 5×10^{-9} A cm^{-2} below 20 V as well as an avalanche gain exceeding 100 have been achieved.

GaN p-i-n APDs fabricated on bulk GaN substrates have been demonstrated with an optical gain of 10^4 at 280 nm under front illumination, dark current densities below 10^{-7} A cm^{-2} up to 45 V, and breakdown voltage of about 92 V, which

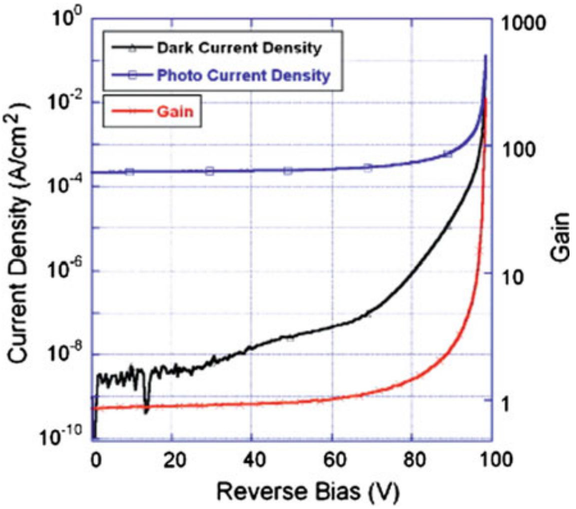

Fig. 9.17 *I–V* characteristics of a front-illuminated homoepitaxial GaN APD (p-i-n) in the dark and under illumination; the multiplication gain is also shown on the *right axis*. Reprinted from [113], Copyright (2008), with permission from Elsevier

corresponds to 2.6 MV cm^{-2} for this structure [111]. For a number of AlGaN APDs, a broadening of the responsivity edge near cut-off was found at elevated reverse bias voltage [112, 114, 115]. This can be attributed to the Franz–Keldysh-Effect, but also an impurity-related absorption band located in the depleted part of the p-GaN at the p-i junction is suggested to be involved in such behavior.

For stable operation of APDs in Geiger-mode—i.e., at a certain over-voltage above breakdown—spatially uniform multiplication regions, free of microplasmas due to defects in the material, are essential. An APD then can be temporarily over-biased with μs-pulses to avoid a large multiplication of the dark current [116]. This enables photon-counting measurements with sufficient gain, where usually PMTs are used. In such experiments, instead of EQE and dark current, the photon detection efficiency (PDE), which is determined by the ratio between recorded and incident pulses, and the dark count rate, i.e., the average number of counts per second, give the significant figures-of-merit. In the year 2000, HVPE grown GaN π-i-n APDs have been demonstrated at 300 K with a PDE of 13 % at 325 nm and a dark count rate of 400 kHz [117]. Also solar-blind AlGaN-based p-i-n APDs have been fabricated and a multiplication gain of 700 at 60 V reverse bias was obtained [118].

Recent results on the performance of back-illuminated separate absorption and multiplication (SAM) AlGaN solar-blind APDs of p-i-n-i-n structure showed a low dark current density of 1.06×10^{-8} A cm^{-2} at 20 V reverse bias and a multiplication gain of about 3000 at 91 V [115]. An even higher gain of 1.2×10^4 at 84 V reverse bias was realized recently by Zhen et al. exploiting the higher ionization coefficient for holes along the (0001) direction of wurtzite GaN mentioned above, in a SAM structure (p-i-n-i-n) in the back-illuminated configuration [119]. Although these and comparable results promise AlGaN-based APDs to be superior to PMTs or Si-based photon-counting units, besides the AlGaN APD also the readout electronics have to be considered. It means, even if the background noise is low for a wide-bandgap detector, the readout circuit noise may limit the measurement of single photons in a given sampling time. Hence, rather than the NEP, the number of rms noise equivalent electrons with no signal incident is considered as figure-of-merit to properly design a photon-counting sensor [120].

The effects of polarization on the device characteristics of a back-illuminated AlGaN SAM PD have been modeled by Dong et al. [121]. According to their analysis, an increase in Al mole fraction of the p-AlGaN layer results in a significant reduction of avalanche breakdown voltage of the APDs. Moreover, the introduction of a polarization-induced electric field in the multiplication region leads to an increase in multiplication gain. Finally, by utilizing the polarization-doping effect in the p-type AlGaN layer, the simulated maximum gain of the APDs could further be increased.

As pointed out above, the p-i-n PD is the basis of the APD or the SAM PD. In order to meet the conditions of photon-counting applications, due to the structural complexity on the one hand, and the requirement of well-defined as well as homogeneous high-field regions on the other hand, the highest level of device reliability has to be achieved. However, the scientific results presented clearly prove the possibility to obtain outstanding performance utilizing AlGaN-based APDs—even in a wide range of the UV.

9.3.6 AlGaN-Based Photocathode

For clean n- and p-GaN(0001) surfaces Eyckeler et al. experimentally derived work functions of 3.88 and 3.6 eV and revealed the existence of depletion and inversion layers, respectively [122]. An exposure of p-GaN to oxygen followed by Cs deposition was found to lower the vacuum level to about 0.7 eV below the bulk conduction band minimum—i.e., a negative electron affinity (NEA) results [123].

Machuca et al. investigated the oxygen species in Cs/O activated p-type GaN NEA photocathodes utilizing synchrotron radiation photoemission spectroscopy to monitor the oxygen during the activation of NEA as well as during operation of the photocathode under UHV conditions [124]. An ion of molecular oxygen was found to be the dominant chemical species of oxygen in the thin Cs/O adlayer that activates the GaN surface. After about 10 h of UV illumination, a decay of the QE from ~ 20 % to less than 10 % within further 7.5 h was observed. An analysis of the valence band and core level states revealed a physical alteration of the Cs/O layer causing a change in the electronic structure of the initial di-oxygen from a -2 charge state to the -1 charge state during the QE shift.

Siegmund et al. reported about the stability of their p-GaN (Cs) photocathodes [125]. The QE has not vanished after an atmospheric pressure N_2 exposure and can be recovered to >50 % of the initial QE by a vacuum bakeout at 200 °C. Only the long wavelength QE near cut-off is found to be significantly changed, as assumed from electron surface escape characteristics. A photocathode in a sealed tube was

Fig. 9.18 Spectra of external quantum efficiency for a photocathode device taken over a 3 year period, no significant aging is observed. Reprinted from [125], Copyright (2006), with permission from Elsevier

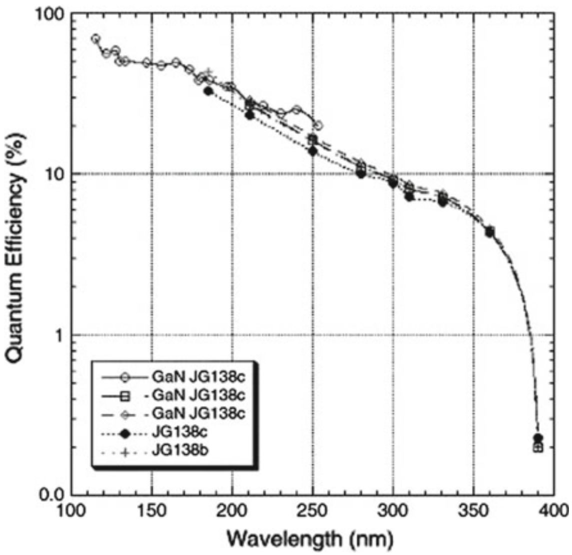

found to be stable over 3 years, as shown in Fig. 9.18, and samples measured in a process tank at 10^{-9} Torr did not degrade over a 6-month period. They also pointed out that this level of stability is better in comparison to that of common cathode materials, e.g., made of CsI or CsTe.

Visible-blind phototubes based on cesiated p-GaN photocathodes have been fabricated [126]. The NEA cathode sample of 0.5 × 0.3 cm^2 area was placed opposed to a 1-mm-thick wire loop anode in a sealed glass tube of 2 cm diameter and 7 cm length. In this configuration, a QE of 30 % at 200 nm wavelength and VIS/UV rejection of up to four orders of magnitude have been measured. The authors also claimed a long-term stability of their cesiated cathodes, since the measured QE changed less than 1 % within a storage duration of two months. In addition, an increase in QE with p-type conductivity of the material was reported. This indicates difficulties for material with high Al content, since the higher acceptor ionization energy then causes the QE to be reduced, accordingly.

The electron affinity of a clean AlN surface was found to be $\chi_{\mathrm{AlN}} \approx 1.9$ eV and Cs adsorption then led to a true NEA with $\chi_{\mathrm{Cs/AlN}} \approx -0.7$ eV [123, 127, 128], but no data on the performance of AlN photocathodes has been reported so far.

In conclusion, the QE values of p-GaN photocathodes range from about 10 % at the threshold wavelength [125] to about 72 % at 230 nm [129]. For the p-type AlGaN-based photocathode, the doping issues hold, as for the Schottky and p-i-n PD. Finally, the chemical instability of the Cs adlayer remains the main obstacle that needs to be solved in the future, especially in terms of device degradation. However, the integration in an electron-multiplying setup can be done straight forward, based on mature technologies.

9.3.7 III-Nitride-Based Devices of High Integration Level

Since the first report on visible-blind GaN-based 32 × 32 pixel focal-plane-array (FPA) cameras, consisting of GaN/AlGaN p-i-n photodiodes hybridized to silicon readout integrated circuits (ROICs) [130, 131], further GaN or AlGaN FPAs in linear [132, 133] and two-dimensional arrangement have been realized. The main detector types, such as Schottky diodes [132, 134], MSM detectors [132] and p-i-n diodes [74, 135] were fabricated and the standard characterization results, similar to those of the single devices mentioned above, showed that visible-blind as well as solar-blind 2D-imaging with 8 × 8 [136], 128 × 128 [137], 256 × 256 [74] or even 320 × 256 [104, 137–140] pixels is possible (see Fig. 9.19).

However, lattice mismatch and defects are a challenge to such large-area devices. Recently, Cicek et al. reported on an effective approach to reduce the number of cracks in solar-blind p-i-n based FPA imaging strucures by utilizing reduced area epitaxy [141]. With this approach, 97 % of the pixels were obtained crack-free and showed an enhancement of about 10 % in the peak EQE compared to devices on a conventionally grown reference sample. However, the prepatterning procedure of the AlN template prior to device growth led to a reduction of the pixel fill-factor to about 48 % (22 μm × 22 μm total device at 30 μm × 30 μm periodicity) compared to 73 % achievable by conventional mesa-structuring the whole p-i-n device [104].

In the design of such FPA systems, flip-chip mounting is usually utilized to integrate the AlGaN photodetector via In-bump technology with a Si readout integrated circuit (ROIC) chip. As already mentioned, back-illumination of a PD results in the limitation of the response to wavelengths above the respective cut-off from any radiation filtering layers, such as substrates, which is crucial for the detection of VUV radiation below about 140 nm. The removal of a sapphire substrate requires high mechanical stresses and may cause harmful damage of the thin remaining device layers. To overcome these difficulties, Malinowski et al.

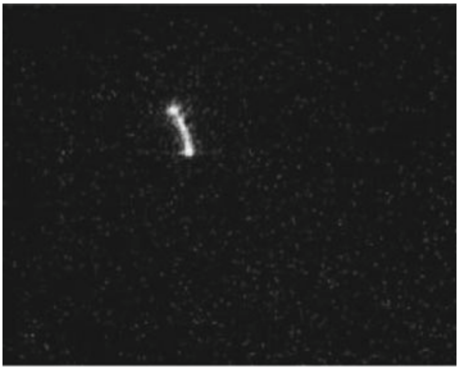

Fig. 9.19 Electric arc recorded with a solar-blind FPA camera with 320 × 256 pixels. Reprinted with permission from [138], Copyright 2005, AIP Publishing LLC

fabricated 400-nm-thick AlGaN membranes by locally etching away the Si(111) substrate after face-down integration to a Si-ROIC [134]. The individual solar-blind Schottky PDs of the 7 × 3 array showed the capability for solar-blind detection with high VIS/UV rejection.

In conclusion, the integration of AlGaN-based photodetectors to ROICs has already been realized at a comparably early stage in III-Nitride photodetector research. Useful processing steps and techniques have been successfully employed in order to enhance the yield of individual PDs making up such large-scale devices.

9.4 Present Status of Wide Bandgap Photodetectors

During the 1980’s, there have been developments in GaN and AlGaN growth that led to different patents mainly on the epitaxy of single layers [142–151]. Although, subsequently more patents on complete photodetector structures were released [152–154] and new materials—such as several oxides like TiO_2, SnO_2, ZrO_2, or ZnO—emerged [155, 156], the work on improvement of material quality is a key issue in the field of UV photodetectors up to now [157, 158]. This incomplete listing is meant to give a brief overview of the companies dealing with UV photodiodes.[13] In 1993 APA OPTICS Inc. filed a patent on GaN and AlGaN-based photoconductors [159]. In 2000, there have been patents by SANYO on a Pd-Schottky electrode on an n-SiC substrate [160] and by APA OPTICS Inc. on a 8 × 8 Schottky-type photodetector array based on GaN with a pixel size of 200 μm by 200 μm [161]. The next year, General Electric patented a photodetector based on homoepitaxial GaN having a dislocation density below 10^5 cm^{-2} [162]. In 2002, a Schottky PD based on metal-oxides—TiO_2, ZnO, SnO_2, SiO_2, ZrO_2, PbO, MnO, Fe_2O_3, or In_2O_3—with a Schottky contact made of Pt, Pd, Ni, Au, or Ag was claimed by the company sglux [155]. In 2005, Hamamatsu filed a patent on a back-illuminated photodiode array for computed tomography [163] and OSAKA GAS CO. LTD. filed a patent on a flame sensor based on an AlGaN p-i-n photodiode using a GaN-layer process with ELO [164]. In 2007, Iwate Information System Corp. filed a patent on a UV PD based on ZnO substrate and AlGaN active layer [156]. Also in 2008, Canon filed a patent on a Schottky photodiode with a periodic concavo-convex structured surface for higher efficiency [165] and NEC filed a patent on a back-illuminated Schottky photodiode with a surface plasmon periodic structure to combine sensitivity and speed [166]. In July 2010, Hamamatsu released the first GaN-based transmission photocathode for the UV range [167, 168]. In 2012, Lai et al. released a paper and a patent on a solar-blind Schottky diode based on Au/wurzite MgS/n^+-GaAs (111) substrate [169, 170]. This detector has a cut-off at 240 nm and shows an EQE of 10 % at a peak wavelength of 225 nm.

---

[13] Companies like: Kyosemi Corporation, Hamamatsu Photonics K.K., SANYO Electric Co. Ltd., General Electric Company, Cree Inc., and others.

Table 9.1 Typical parameters of commercially available photodetectors

Material [Ref.] Type	A_{sens} (mm^2)	$\Delta\lambda$ λ_{peak} (nm)	Rsp at λ, U_{rev} (mA W^{-1})	I_{dark} at U_{rev} (pA)	NEP at λ (W/$\sqrt{\mathrm{Hz}}$)	$\tau_{\mathrm{rise}}/\tau_{\mathrm{fall}}$ (ns)	C_{t} at 0 V (pF)
GaP [172]	1.2	150–550	28	10	1.1×10^{-14}	1/20	300
Schottky		440	254 nm, 5 V	5 V	440 nm		
CsTe [173]	78.5	160–320	1.4×10^{7}	300		2.5/24	2
PMT		240	254 nm, 1 kV	1 kV			
TiO_2 [174]	4.18	215–385	21	30			1000
Schottky		300	300 nm, 3 V	1 V			
ZnO [175]		225–380	2600			10/960	
Photoconductor[a]		370	370 nm, 10 V				
GaN [176]		200–365	1,500,000	5		300/600	
Photoconductor[a]		365	254 nm, 10 V	10 V			
GaN [177]	0.8	290–365	150	1000			
p-i-n		365	350 nm, 0 V	1 V			
GaN [178]	0.09	230–375	80	50			24
Schottky		365	254 nm, 0 V	1 V			
AlGaN [179]	1.0	150–282	66	5	1.33×10^{-14}	40/60	320
Schottky		260	254 nm, 0 V	1 V	254 nm		
AlGaN [180]	1.536	210–280	50	20			
p-i-n		280	254 nm, 0 V	0.1 V			
AlGaN [181]	0.031	240–278	66.3	145			
APD[a]		260	260 nm, 0 V	20 V			
SiC [182]	0.056	230–285	84	0.005	9×10^{-16}		20
p-i-n		270	254 nm, 0 V	1 V	270 nm		
SiC [183]	1	220–275	80	0.001			195
p-i-n		265	254 nm, 0 V	1 V			

Sensitive area A_{sens}, wavelength λ, spectral range $\Delta\lambda$ ($Rsp \geq 1\,\% Rsp_{\mathrm{max}}$), peak wavelength λ_{peak}, responsivity Rsp, reverse bias voltage U_{rev}, dark current I_{dark}, noise-equivalent-power NEP, rise and fall times $\tau_{\mathrm{rise,fall}}$ (10–90 %), and the device capacitance C_t

[a] Not commercially available, scientific reports (for comparison only)

In 2013, NEC filed a patent on a waveguide-coupled MSM photodetector based on GaN. The reduced light reflection at the MSM electrode improves the efficiency, so that the bias voltage can be reduced [171].

In Table 9.1 different types of UV photodetectors are listed, which are based on several material systems and have an active area between 0.031 and 78.5 mm^2. Except for the GaP Schottky PD, all PDs operate solely in the UV, showing peak wavelengths between 370 and 240 nm, and thus are suitable for applications requiring visible-blind or even solar-blind detection capabilities. For the PDs based on $Al_xGa_{1-x}N$, that can be operated at zero bias, the responsivities range between 60 to 150 mA W^{-1}, which is competitive to SiC-based p-i-n PDs having about 80 mA W^{-1}. Except the GaN as well as the ZnO photoconductor with their enhanced responsivities at 10 V bias, values below 28 mA W^{-1} are achieved with GaP Schottky PDs, and TiO_2 Schottky PD at a small bias voltage. In comparison to that, the CsTe PMT requires a high voltage of 1 kV in order to operate at a responsivity of 1.4×10^7 mA W^{-1} at 254 nm due to the gain of 5×10^5 at this bias. The dark current level of 300 pA for this PMT has been obtained after storing the device for 30 min in the dark. But the very short rise and fall times as well as the low device capacitance for the PMT are remarkable in comparison to all other devices. However, given values for the *NEP* range between 10^{-16} and 10^{-14} cm Hz$^{1/2}$ W^{-1} for the SiC p-i-n PD, the GaP and the $Al_xGa_{1-x}N$ Schottky PDs promising high performance in detecting low power levels.

We conclude, that in comparison to rather mature technologies in SiC or GaP device fabrication, the $Al_xGa_{1-x}N$-based UV PDs are definitely competitive today, and outstanding performance can be achieved, regardless of the device type.

9.5 Summary and Conclusions

This overview on AlGaN-based UV photodetectors (PDs) covers the simple device types, such as the photoconductor, the metal–semiconductor–metal (MSM) PD and the Schottky PD as well as rather complex p-i-n PDs, avalanche PDs (APDs), separate absorption multiplication PDs (SAM PDs), their integration as 1D- or even 2D-arrays, and AlGaN photocathode material for photomultiplier tubes (PMTs), which were developed within the last two decades. According to the different device structures and designs on the one hand, and the challenges in the epitaxy of $Al_xGa_{1-x}N$ layer structures as well as related processing issues on the other hand, a variety of performance data was reported.

The high photocurrents observed for GaN photoconductors with ohmic contacts usually correlate with photoconductive gain which results in a low frequency bandwidth, whereas the easy-to-fabricate MSM PD with two blocking contacts on an non-intentionally doped AlGaN layer can achieve low dark current levels and also high detection capability by utilizing a suitable electrode geometry. Since these devices rely on an applied bias voltage, the Schottky PD as well as the p-i-n PD constitute very attractive alternatives, because they can be operated in zero bias mode. In general the p-i-n design offers a potentially higher stability compared to the Schottky PD, since electric fields can be controlled by the properties of the i-layer. But in order to tailor, the whole UV range from the UV-A to the UV-C or even the VUV with the p-i-n design, p- or n-type $Al_xGa_{1-x}N$ material with arbitrary Al mole fraction x_{Al} of high quality is required. However, even today the doping of AlGaN and the processing of ohmic contacts to AlGaN layers are not straight forward, especially with rising x_{Al}. Therefore, only the MSM PD and the Schottky PD could be fabricated on AlN layers with a corresponding cut-off wavelength λ_c of about 200 nm (VUV). Nevertheless, very efficient solar-blind ($\lambda_c = 280$ nm) p-i-n PDs were obtained by utilizing complex heterostructure designs and the concept of backside illumination. For all these device types, typical values for the external quantum efficiency (EQE) range between several 10 % and about 90 % below breakdown without the indication of any gain mechanism. Moreover, AlGaN-based APDs and even SAM PDs were realized enabling photon-counting measurements that prove competitive performance of AlGaN-based APDs to conventional PMTs. Also the successful processing of Schottky PDs and p-i-n PDs on the wafer-level to form 1D or 2D focal-plane arrays integrated into read-out circuits was demonstrated. Although, the p-GaN photocathode material developed may suffer from chemical alterations of the cesiated surface under UV illumination, and a decreasing EQE for higher x_{Al} (supposed to correlate to the increasing acceptor ionization energy), the overall performance of photocathodes obtained shows very promising results.

In conclusion, $Al_xGa_{1-x}N$-based photodetectors have been realized in a variety of device types which for some applications offer advantages over devices made from other materials, such as Si, SiC, and GaP. Although there is still room for improvement concerning material quality and process technology, $Al_xGa_{1-x}N$-based PDs are already commercially available. Especially the large and tunable band gap energies, resulting in high radiation hardness and enabling custom-made cut-off wavelengths, make $Al_xGa_{1-x}N$-based photodetectors promising candidates for solar-blind and visible-blind photodetection in UV applications.

References

1. I. Vurgaftman, J.R. Meyer, L.R. Ram-Mohan, Band parameters for III-V compound semiconductors and their alloys. J. Appl. Phys. **89**(11), 5815–5875 (2001)
2. S. Einfeldt, V. Kirchner, H. Heinke, M. Dießelberg, S. Figge, K. Vogeler, D. Hommel, Strain relaxation in AlGaN under tensile plane stress. J. Appl. Phys. **88**(12), 7029–7036 (2000)
3. M. Asif Khan, R.A. Skogman, J.M. Van Hove, D.T. Olson, J.N. Kuznia, Atomic layer epitaxy of GaN over sapphire using switched metalorganic chemical vapor deposition. Appl. Phys. Lett. **60**(11), 1366–1368 (1992)
4. E. Valcheva, T. Paskova, G. Radnoczi, L. Hultman, B. Monemar, H. Amano, and I. Akasaki, Growth-induced defects in AlN/GaN superlattices with different periods. Phys. B: Condens. Matter **340–342**(0), 1129–1132 (2003). (Proceedings of the 22nd international conference on defects in semiconductors)

5. J.P. Zhang, H.M. Wang, M.E. Gaevski, C.Q. Chen, Q. Fareed, J.W. Yang, G. Simin, M.A. Khan, Crack-free thick AlGaN grown on sapphire using AlN/AlGaN superlattices for strain management. Appl. Phys. Lett. **80**(19), 3542–3544 (2002)
6. K. Nagamatsu, N. Okada, H. Sugimura, H. Tsuzuki, F. Mori, K. Iida, A. Bando, M. Iwaya, S. Kamiyama, H. Amano, I. Akasaki, High-efficiency AlGaN-based UV light-emitting diode on laterally overgrown AlN. J. Cryst. Growth **310**(7–9), 2326–2329 (2008). (The Proceedings of the 15th international conference on crystal growth (ICCG-15) in conjunction with the international conference on vapor growth and epitaxy and the US Biennial workshop on organometallic vapor phase epitaxy)
7. H. Hirayama, S. Fujikawa, J. Norimatsu, T. Takano, K. Tsubaki, N. Kamata, Fabrication of a low threading dislocation density ELO-AlN template for application to deep-UV LEDs. Phys. Status Solidi (C) **6**(S2), S356–S359 (2009)
8. V. Kueller, A. Knauer, C. Reich, A. Mogilatenko, M. Weyers, J. Stellmach, T. Wernicke, M. Kneissl, Z. Yang, C. Chua, N. Johnson, Modulated epitaxial lateral overgrowth of AlN for efficient UV LEDs. IEEE Photonics Technol. Lett. **24**, 1603–1605 (2012)
9. H. Harima, T. Inoue, S. Nakashima, M. Ishida, M. Taneya, Local vibrational modes as a probe of activation process in p-type GaN. Appl. Phys. Lett. **75**(10), 1383–1385 (1999)
10. S. Nakamura, N. Iwasa, M. Senoh, T. Mukai, Hole compensation mechanism of p-type GaN films. Jpn. J. Appl. Phys. **31**(Part 1, No. 5A), 1258–1266 (1992)
11. S. Nakamura, T. Mukai, M. Senoh, N. Iwasa, Thermal annealing effects on p-type mg-doped GaN films. Jpn. J. Appl. Phys. **31**(Part 2, No. 2B), L139–L142 (1992)
12. H. Obloh, K. Bachem, U. Kaufmann, M. Kunzer, M. Maier, A. Ramakrishnan, P. Schlotter, Self-compensation in mg doped p-type GaN grown by MOCVD. J. Cryst. Growth **195**(1–4), 270–273 (1998)
13. U. Kaufmann, M. Kunzer, M. Maier, H. Obloh, A. Ramakrishnan, B. Santic, P. Schlotter, Nature of the 2.8 eV photoluminescence band in mg doped GaN. Appl. Phys. Lett. **72**(11), 1326–1328 (1998)
14. M.L. Nakarmi, N. Nepal, J.Y. Lin, H.X. Jiang, Photoluminescence studies of impurity transitions in Mg-doped AlGaN alloys. Appl. Phys. Lett. **94**(9) (2009)
15. K.B. Nam, M.L. Nakarmi, J. Li, J.Y. Lin, H.X. Jiang, Mg acceptor level in AlN probed by deep ultraviolet photoluminescence. Appl. Phys. Lett. **83**(5), 878–880 (2003)
16. M.L. Nakarmi, N. Nepal, C. Ugolini, T.M. Altahtamouni, J.Y. Lin, H.X. Jiang, Correlation between optical and electrical properties of mg-doped AlN epilayers. Appl. Phys. Lett. **89** (15) (2006)
17. Q. Liu, S. Lau, A review of the metal-GaN contact technology. Solid-State Electron. **42**(5), 677–691 (1998)
18. S. Pal, T. Sugino, Fabrication and characterization of metal/GaN contacts. Appl. Surf. Sci. **161**(1–2), 263–267 (2000)
19. V.M. Bermudez, Study of oxygen chemisorption on the GaN(0001)-(1×1) surface. J. Appl. Phys. **80**(2), 1190–1200 (1996)
20. Q.Z. Liu, S.S. Lau, N.R. Perkins, T.F. Kuech, Room temperature epitaxy of Pd films on GaN under conventional vacuum conditions. Appl. Phys. Lett. **69**(12), 1722–1724 (1996)
21. S.J. Pearton, J.C. Zolper, R.J. Shul, F. Ren, GaN: Processing, defects, and devices. J. Appl. Phys. **86**(1), 1–78 (1999)
22. M. Razeghi, A. Rogalski, Semiconductor ultraviolet detectors. J. Appl. Phys. **79**(10), 7433–7473 (1996)
23. E. Muñoz, E. Monroy, J.L. Pau, F. Calle, F. Omnès, P. Gibart, III nitrides and UV detection. J. Phys.: Condens. Matter **13**(32), 7115 (2001)
24. M. Razeghi, Short-wavelength solar-blind detectors-status, prospects, and markets. Proc. IEEE **90**, 1006–1014 (2002)
25. M.A. Khan, M. Shatalov, H.P. Maruska, H.M. Wang, E. Kuokstis, III-nitride UV devices. Jpn. J. Appl. Phys. **44**(10R), 7191 (2005)
26. E. Muñoz, (Al,In,Ga)N-based photodetectors. some materials issues. Phys. Status Solidi (b) **244**(8), 2859–2877 (2007)

27. Wide bandgap UV photodetectors: a short review of devices and applications **6473** (2007)
28. L. Sang, M. Liao, M. Sumiya, A comprehensive review of semiconductor ultraviolet photodetectors: From thin film to one-dimensional nanostructures. Sensors **13**(8), 10482–10518 (2013)
29. R. Bube, *Photoconductivity of solids* (Wiley, 1960)
30. H. Tholl, *Bauelemente der Halbleiterelektronik: Teil 2 Feldeffekt-Transistoren, Thyristoren und Optoelektronik (Leitfaden der Elektrotechnik) (German Edition)*, (Vieweg+Teubner Verlag, 1978)
31. G. Winstel, C. Weyrich, *Optoelektronik II: Photodioden* (Phototransistoren, Photoleiter und Bildsensoren (Halbleiter-Elektronik) (German Edition), Springer, 1986)
32. P. Dennis, *Photodetectors: an introduction to current technology* (Springer, 1986)
33. J. Geist, Planar silicon photosensors. In: *Sensor Technology and Devices (Optoelectronics Library)*, ed. by L. Ristic (Artech House Publishers, 1994)
34. K.K. Ng, *Complete Guide to Semiconductor Devices* (McGraw-Hill Education (ISE Editions), 1995)
35. S.M. Sze, K.K. Ng, *Physics of Semiconductor Devices* (Wiley-Interscience, 2006)
36. J.I. Pankove, H.P. Maruska, J.E. Berkeyheiser, Optical absoption of GaN. Appl. Phys. Lett. **17**(5), 197–199 (1970)
37. D.E. Aspnes, A.A. Studna, Dielectric functions and optical parameters of Si, Ge, GaP, GaAs, GaSb, InP, InAs, and InSb from 1.5 to 6.0 eV. Phys. Rev. B **27**, 985–1009 (1983)
38. M.D. Sturge, Optical absorption of gallium arsenide between 0.6 and 2.75 eV. Phys. Rev. **127**, 768–773 (1962)
39. S. Zollner, J.G. Chen, E. Duda, T. Wetteroth, S.R. Wilson, J.N. Hilfiker, Dielectric functions of bulk 4 h and 6 h SiC and spectroscopic ellipsometry studies of thin SiC films on Si. J. Appl. Phys. **85**(12), 8353–8361 (1999)
40. V. Srikant, D.R. Clarke, Optical absorption edge of ZnO thin films: the effect of substrate. J. Appl. Phys. **81**(9), 6357–6364 (1997)
41. M. Röppischer, *Optische Eigenschaften von Aluminium-Galliumnitrid-Halbleitern* (Südwestdeutscher Verlag für Hochschulschriften, Saarbrücken, 2011)
42. H.R. Phillip, E.A. Taft, Kramers-Kronig analysis of reflectance data for diamond. Phys. Rev. **136**, A1445–A1448 (1964)
43. A.D. Papadopoulos, E. Anastassakis, Optical properties of diamond. Phys. Rev. B **43**, 5090–5097 (1991)
44. E. Palik, *Handbook of Optical Constants of Solids, Volumes I, II, and III: Subject Index and Contributor Index.* Academic Press Handbook Series (Elsevier Science & Technology, 1985)
45. R. Kohlrausch, Theorie des elektrischen Rückstandes in der Leidener Flasche. Ann. Phys. **167**(1), 56–82 (1854)
46. J. Phillips, Kohlrausch relaxation and glass transitions in experiment and in molecular dynamics simulations. J. Non-Cryst. Solids **182**(1–2), 155–161 (1995)
47. M. Cardona, R. Chamberlin, W. Marx, The history of the stretched exponential function. Ann. Phys. **16**(12), 842–845 (2007)
48. M. Brendel, *Build-up and decay transient of a GaN MSM photodetector showing persistent photoconductivity (PPC).* Unpublished data from Ferdinand-Braun-Institut, Leibniz-Intitut für Höchstfrequenztechnik (FBH)
49. J.A. Garrido, E. Monroy, I. Izpura, E.M. Noz, Photoconductive gain modelling of GaN photodetectors. Semicond. Sci. Technol. **13**(6), 563 (1998)
50. C.H. Park, D.J. Chadi, Stability of deep donor and acceptor centers in GaN, AlN, and BN. Phys. Rev. B **55**, 12995–13001 (1997)
51. V.V. Ursaki, I.M. Tiginyanu, P.C. Ricci, A. Anedda, S. Hubbard, D. Pavlidis, Persistent photoconductivity and optical quenching of photocurrent in GaN layers under dual excitation. J. Appl. Phys. **94**(6), 3875–3882 (2003)
52. O. Katz, V. Garber, B. Meyler, G. Bahir, J. Salzman, Gain mechanism in GaN schottky ultraviolet detectors. Appl. Phys. Lett. **79**(10), 1417–1419 (2001)
53. K.K. Hamamatsu Photonics, Si photodiodes

54. R. Müller, *Rauschen: Zweite, überarbeitete und erweiterte Auflage (Halbleiter-Elektronik) (Volume 15) (German Edition)* (Springer, 1989)
55. E. Rhoderick, R. Williams, *Metal-semiconductor contacts*, Monographs in electrical and electronic engineering (Clarendon Press, 1988)
56. R.T. Tung, The physics and chemistry of the schottky barrier height. Appl. Phys. Rev. **1**(1) (2014)
57. K. Böer, *Introduction to space charge effects in semiconductors.* Springer Series in Solid-State Sciences (Springer, 2009)
58. S.M. Sze, D.J. Jr Coleman, A. Loya, Current transport in metal-semiconductor-metal (MSM) structures. Solid-State Electron. **14**(12), 1209–1218 (1971)
59. A. Sarto, B. Van Zeghbroeck, Photocurrents in a metal-semiconductor-metal photodetector. IEEE J. Quantum Electron. **33**, 2188–2194 (1997)
60. S. Chou, M.Y. Liu, Nanoscale tera-hertz metal-semiconductor-metal photodetectors. IEEE J. Quantum Electron. **28**, 2358–2368 (1992)
61. Z. Marks, B. Van Zeghbroeck, High-speed nanoscale metal-semiconductor-metal photodetectors with terahertz bandwidth. In: 2010 10th International Conference on Numerical Simulation of Optoelectronic Devices (NUSOD) (2010), pp. 11–12
62. I.H. Oguzman, E. Bellotti, K.F. Brennan, J. Kolnk, R. Wang, P.P. Ruden, Theory of hole initiated impact ionization in bulk zincblende and wurtzite GaN. J. Appl. Phys. **81**(12), 7827–7834 (1997)
63. B.E.A. Saleh, M.C. Teich, *Fundamentals of Photonics* (Wiley, 2007)
64. W.E. Spicer, The use of photoemission to determine the electronic structure of solids. J. Phys. Colloques **34**, C6–19–C6–33 (1973)
65. W.E. Spicer, Photoemissive, photoconductive, and optical absorption studies of alkali-antimony compounds. Phys. Rev. **112**, 114–122 (1958)
66. W.E. Spicer, Photoemission and related properties of the alkali-antimonides. J. Appl. Phys. **31**(12), 2077–2084 (1960)
67. C.N. Berglund, W.E. Spicer, Photoemission studies of copper and silver: Theory. Phys. Rev. **136**, A1030–A1044 (1964)
68. J. Scheer, J. van Laar, GaAs-Cs: A new type of photoemitter. Solid State Commun. **3**(8), 189–193 (1965)
69. Y. Sun, R.E. Kirby, T. Maruyama, G.A. Mulhollan, J.C. Bierman, P. Pianetta, The surface activation layer of GaAs negative electron affinity photocathode activated by Cs, Li, and NF3. Appl. Phys. Lett. **95**(17) (2009)
70. E. Pertzsch, Responsivity spectra: Comparison between several AlGaN-based photodetectors and SiC as well as GaP photodetectors. Unpublished data from JENOPTIK Polymer Systems GmbH (JOPS)
71. J.I. Pankove, J.E. Berkeyheiser, Properties of Zn-doped GaN. II. Photoconductivity. J. Appl. Phys. **45**(9), 3892–3895 (1974)
72. H.P. Maruska, J.J. Tietjen, The preparation and properties of vapor-deposited single-crystalline GaN. Appl. Phys. Lett. **15**(10), 327–329 (1969)
73. M.A. Khan, J.N. Kuznia, D.T. Olson, J.M. Van Hove, M. Blasingame, L.F. Reitz, High-responsivity photoconductive ultraviolet sensors based on insulating single-crystal GaN epilayers. Appl. Phys. Lett. **60**(23), 2917–2919 (1992)
74. P. Lamarre, A. Hairston, S. Tobin, K. Wong, A. Sood, M. Reine, M. Pophristic, R. Birkham, I. Ferguson, R. Singh, C. Eddy, U. Chowdhury, M. Wong, R. Dupuis, P. Kozodoy, E. Tarsa, AlGaN UV focal plane arrays. Phys. Status Solidi (A) **188**(1), 289–292 (2001)
75. F. Binet, J.Y. Duboz, E. Rosencher, F. Scholz, V. Haerle, Mechanisms of recombination in GaN photodetectors. Appl. Phys. Lett. **69**(9), 1202–1204 (1996)
76. E. Monroy, F. Calle, J.A. Garrido, P. Youinou, E. Muñoz, F. Omnès, B. Beaumont, P. Gibart, Si-doped $Al_xGa_{1-x}N$ photoconductive detectors. Semicond. Sci. Technol. **14**(8), 685 (1999)

77. D. Walker, X. Zhang, A. Saxler, P. Kung, J. Xu, M. Razeghi, $Al_xGa_{1-x}N$ ($0 \leq x \leq 1$) ultraviolet photodetectors grown on sapphire by metal-organic chemical-vapor deposition. Appl. Phys. Lett. **70**(8), 949–951 (1997)
78. T.D. Moustakas, M. Misra, Origin of the high photoconductive gain in AlGaN films. Proc. SPIE **6766** (2007)
79. K.S. Stevens, M. Kinniburgh, R. Beresford, Photoconductive ultraviolet sensor using Mg-doped GaN on Si(111). Appl. Phys. Lett. **66**(25), 3518–3520 (1995)
80. P. Kung, X. Zhang, D. Walker, A. Saxler, J. Piotrowski, A. Rogalski, M. Razeghi, Kinetics of photoconductivity in n-type GaN photodetector. Appl. Phys. Lett. **67**(25), 3792–3794 (1995)
81. C. Johnson, J.Y. Lin, H.X. Jiang, M.A. Khan, C.J. Sun, Metastability and persistent photoconductivity in Mg-doped p-type GaN. Appl. Phys. Lett. **68**(13), 1808–1810 (1996)
82. H.M. Chen, Y.F. Chen, M.C. Lee, M.S. Feng, Persistent photoconductivity in n-type GaN. J. Appl. Phys. **82**(2), 899–901 (1997)
83. J. Carrano, T. Li, P. Grudowski, C. Eiting, R. Dupuis, J. Campbell, High quantum efficiency metal-semiconductor-metal ultraviolet photodetectors fabricated on single-crystal GaN epitaxial layers. Electron. Lett. **33**, 1980–1981 (1997)
84. J.C. Carrano, T. Li, D.L. Brown, P.A. Grudowski, C.J. Eiting, R.D. Dupuis, J.C. Campbell, Very high-speed metal-semiconductor-metal ultraviolet photodetectors fabricated on GaN. Appl. Phys. Lett. **73**(17), 2405–2407 (1998)
85. B. Yang, D.J.H. Lambert, T. Li, C. Collins, M. Wong, U. Chowdhury, R. Dupuis, J. Campbell, High-performance back-illuminated solar-blind AlGaN metal-semiconductor-metal photodetectors. Electron. Lett. **36**, 1866–1867 (2000)
86. M. Brendel, M. Helbling, A. Knauer, S. Einfeldt, A. Knigge, M. Weyers, Top- and bottom-illumination of solar-blind AlGaN metal-semiconductor-metal photodetectors. Phys. Status Solidi (A) (2015)
87. F. Xie, H. Lu, D. Chen, X. Ji, F. Yan, R. Zhang, Y. Zheng, L. Li, J. Zhou, Ultra-low dark current AlGaN-based solar-blind metal-semiconductor-metal photodetectors for high-temperature applications. IEEE Sens. J. **12**, 2086–2090 (2012)
88. J. Li, Z.Y. Fan, R. Dahal, M.L. Nakarmi, J.Y. Lin, H.X. Jiang, 200 nm deep ultraviolet photodetectors based on AlN. Appl. Phys. Lett. **89**(21) (2006)
89. A. Knigge, M. Brendel, F. Brunner, S. Einfeldt, A. Knauer, V. Kueller, M. Weyers, AlGaN photodetectors for the UV-C spectral region on planar and epitaxial laterally overgrown AlN/sapphire templates. Phys. Status Solidi (C) **10**(3), 294–297 (2013)
90. M. Brendel, A. Knigge, F. Brunner, S. Einfeldt, A. Knauer, V. Kueller, U. Zeimer, M. Weyers, Anisotropic responsivity of AlGaN metalsemiconductormetal photodetectors on epitaxial laterally overgrown AlN/sapphire templates. J. Electron. Mater. **43**(4), 833–837 (2014)
91. M. Asif Khan, J.N. Kuznia, D.T. Olson, M. Blasingame, A.R. Bhattarai, Schottky barrier photodetector based on Mg-doped p-type GaN films. Appl. Phys. Lett. **63**(18), 2455–2456 (1993)
92. A.C. Schmitz, A.T. Ping, M.A. Khan, Q. Chen, J.W. Yang, I. Adesida, Schottky barrier properties of various metals on n-type GaN. Semicond. Sci. Technol. **11**(10), 1464 (1996)
93. Q. Chen, J.W. Yang, A. Osinsky, S. Gangopadhyay, B. Lim, M.Z. Anwar, M. Asif Khan, D. Kuksenkov, H. Temkin, Schottky barrier detectors on GaN for visible-blind ultraviolet detection. Appl. Phys. Lett. **70**(17), 2277–2279 (1997)
94. T. Hashizume, J. Kotani, H. Hasegawa, Leakage mechanism in GaN and AlGaN schottky interfaces. Appl. Phys. Lett. **84**(24), 4884–4886 (2004)
95. K.Y. Park, B.J. Kwon, Y.-H. Cho, S.A. Lee, J.H. Son, Growth and characteristics of Ni-based schottky-type $Al_xGa_{1-x}N$ ultraviolet photodetectors with AlGaN/GaN superlattices. J. Appl. Phys. **98**(12) (2005)
96. H. Miyake, H. Yasukawa, Y. Kida, K. Ohta, Y. Shibata, A. Motogaito, K. Hiramatsu, Y. Ohuchi, K. Tadatomo, Y. Hamamura, K. Fukui, High performance schottky UV detectors (265–100 nm) using n-$Al_{0.5}Ga_{0.5}N$ on AlN epitaxial layer. Phys. Status Solidi (A) **200**(1), 151–154 (2003)

97. R. Dahal, T.M. Al Tahtamouni, Z.Y. Fan, J.Y. Lin, H.X. Jiang, Hybrid AlN/SiC deep ultraviolet schottky barrier photodetectors. Appl. Phys. Lett. **90**(26) (2007)
98. C.J. Collins, T. Li, A.L. Beck, R.D. Dupuis, J.C. Campbell, J.C. Carrano, M.J. Schurman, I. A. Ferguson, Improved device performance using a semi-transparent p-contact AlGaN/GaN heterojunction positive-intrinsic-negative photodiode. Appl. Phys. Lett. **75**(14), 2138–2140 (1999)
99. C. Pernot, A. Hirano, M. Iwaya, T. Detchprohm, H. Amano, I. Akasaki, Solar-blind UV photodetectors based on GaN/AlGaN p-i-n photodiodes. Jpn. J. Appl. Phys. **39**(5A), L387 (2000)
100. T. Li, A.L. Beck, C. Collins, R.D. Dupuis, J.C. Campbell, J.C. Carrano, M.J. Schurman, I.A. Ferguson, Improved ultraviolet quantum efficiency using a semitransparent recessed window AlGaN/GaN heterojunction p-i-n photodiode. Appl. Phys. Lett. **75**(16), 2421–2423 (1999)
101. W. Yang, T. Nohova, S. Krishnankutty, R. Torreano, S. McPherson, H. Marsh, Back-illuminated GaN/AlGaN heterojunction photodiodes with high quantum efficiency and low noise. Appl. Phys. Lett. **73**(8), 1086–1088 (1998)
102. U. Chowdhury, M.M. Wong, C.J. Collins, B. Yang, J.C. Denyszyn, J.C. Campbell, R.D. Dupuis, High-performance solar-blind photodetector using an $Al_{0.6}Ga_{0.4}N$ n-type window layer. J. Cryst. Growth **248**(0), 552–555 (2003). (Proceedings of the eleventh international conference on Metalorga nic Vapor Phase Epitaxy)
103. D.J.H. Lambert, M.M. Wong, U. Chowdhury, C. Collins, T. Li, H.K. Kwon, B.S. Shelton, T. G. Zhu, J.C. Campbell, R.D. Dupuis, Back illuminated AlGaN solar-blind photodetectors. Appl. Phys. Lett. **77**(12), 1900–1902 (2000)
104. E. Cicek, R. McClintock, C.Y. Cho, B. Rahnema, M. Razeghi, $Al_xGa_{1-x}N$-based back-illuminated solar-blind photodetectors with external quantum efficiency of 89 %. Appl. Phys. Lett. **103**(19) (2013)
105. C.J. Collins, U. Chowdhury, M.M. Wong, B. Yang, A.L. Beck, R.D. Dupuis, J.C. Campbell, Improved solar-blind detectivity using an $Al_xGa_{1-x}N$ heterojunction p-i-n photodiode. Appl. Phys. Lett. **80**(20), 3754–3756 (2002)
106. N. Biyikli, I. Kimukin, O. Aytur, E. Ozbay, Solar-blind AlGaN-based p-i-n photodiodes with low dark current and high detectivity. IEEE Photonics Technol. Lett. **16**, 1718–1720 (2004)
107. H. Jiang, T. Egawa, Low-dark-current high-performance AlGaN solar-blind pin photodiodes. Jpn. J. Appl. Phys. **47**(3R), 1541 (2008)
108. A. Hirano, C. Pernot, M. Iwaya, T. Detchprohm, H. Amano, I. Akasaki, Demonstration of flame detection in room light background by solar-blind AlGaN pin photodiode. Phys. Status Solidi (A) **188**(1), 293–296 (2001)
109. J. Kuek, D. Pulfrey, B. Nener, J. Dell, G. Parish, U. Mishra, Effects of polarisation on solar-blind AlGaN UV photodiodes. In Proceedings conference on optoelectronic and microelectronic materials and devices, 2000. COMMAD 2000 (2000), pp. 459–462
110. F. Xie, H. Lu, D. Chen, X. Xiu, H. Zhao, R. Zhang, Y. Zheng, Metal-semiconductor-metal ultraviolet avalanche photodiodes fabricated on bulk GaN substrate. IEEE Electron Device Lett. **32**, 1260–1262 (2011)
111. S.-C. Shen, Y. Zhang, D. Yoo, J.-B. Limb, J.-H. Ryou, P. Yoder, R.D. Dupuis, Performance of deep ultraviolet GaN avalanche photodiodes grown by mocvd. IEEE Photonics Technol. Lett. **19**, 1744–1746 (2007)
112. T. Tut, M. Gokkavas, A. Inal, E. Ozbay, $Al_xGa_{1-x}N$-based avalanche photodiodes with high reproducible avalanche gain. Appl. Phys. Lett. **90**(16) (2007)
113. R.D. Dupuis, J.-H. Ryou, S.-C. Shen, P.D. Yoder, Y. Zhang, H.J. Kim, S. Choi, Z. Lochner, Growth and fabrication of high-performance GaN-based ultraviolet avalanche photodiodes. J. Cryst. Growth **310**(23), 5217–5222 (2008). (The Fourteenth International conference on Metalorganic Vapor Phase Epitax The 14th International conference on Metalorganic Vapor Phase Epitaxy)
114. J.L. Pau, C. Bayram, R. McClintock, M. Razeghi, D. Silversmith, Back-illuminated separate absorption and multiplication GaN avalanche photodiodes. Appl. Phys. Lett. **92**(10) (2008)

115. Y. Huang, D.J. Chen, H. Lu, K.X. Dong, R. Zhang, Y.D. Zheng, L. Li, Z.H. Li, Back-illuminated separate absorption and multiplication AlGaN solar-blind avalanche photodiodes. Appl. Phys. Lett. **101**(25) (2012)
116. R. Mcintyre, On the avalanche initiation probability of avalanche diodes above the breakdown voltage. IEEE Trans. Electron Devices **20**, 637–641 (1973)
117. K.A. McIntosh, R.J. Molnar, L.J. Mahoney, K.M. Molvar, N. Efremow, S. Verghese, Ultraviolet photon counting with GaN avalanche photodiodes. Appl. Phys. Lett. **76**(26), 3938–3940 (2000)
118. R. McClintock, A. Yasan, K. Minder, P. Kung, M. Razeghi, Avalanche multiplication in AlGaN based solar-blind photodetectors. Appl. Phys. Lett. **87**(24) (2005)
119. Z.G. Shao, D.J. Chen, H. Lu, R. Zhang, D.P. Cao, W.J. Luo, Y.D. Zheng, L. Li, Z.H. Li, High-gain AlGaN solar-blind avalanche photodiodes. IEEE Electron Device Lett. **35**, 372–374 (2014)
120. S. Verghese, K.A. McIntosh, R. Molnar, L.J. Mahoney, R. Aggarwal, M. Geis, K. Molvar, E. Duerr, I. Melngailis, GaN avalanche photodiodes operating in linear-gain mode and geiger mode. IEEE Trans. Electron Devices **48**, 502–511 (2001)
121. K.X. Dong, D.J. Chen, H. Lu, B. Liu, P. Han, R. Zhang, Y.D. Zheng, Exploitation of polarization in back-illuminated AlGaN avalanche photodiodes. IEEE Photonics Technol. Lett. **25**, 1510–1513 (2013)
122. M. Eyckeler, W. Mönch, T.U. Kampen, R. Dimitrov, O. Ambacher, M. Stutzmann, Negative electron affinity of cesiated p-GaN(0001) surfaces. J. Vac. Sci. Technol., B **16**(4), 2224–2228 (1998)
123. C.I. Wu, A. Kahn, Electronic states and effective negative electron affinity at cesiated p-GaN surfaces. J. Appl. Phys. **86**(6), 3209–3212 (1999)
124. F. Machuca, Z. Liu, Y. Sun, P. Pianetta, W.E. Spicer, R.F.W. Pease, Oxygen species in Cs/O activated gallium nitride (GaN) negative electron affinity photocathodes. J. Vac. Sci. Technol., B **21**(4), 1863–1869 (2003)
125. O. Siegmund, J. Vallerga, J. McPhate, J. Malloy, A. Tremsin, A. Martin, M. Ulmer, B. Wessels, Development of GaN photocathodes for UV detectors. Nucl. Instrum. Methods Phys. Res. Sect. A: Accelerators, Spectrometers, Detectors Associated Equipment **567**(1), 89–92 (2006). (Proceedings of the 4th international conference on new developments in photodetection BEAUNE 2005 fourth international conference on new developments in photodetection)
126. F. Shahedipour, M. Ulmer, B. Wessels, C. Joseph, T. Nihashi, Efficient GaN photocathodes for low-level ultraviolet signal detection. IEEE J. Quant. Electron. **38**, 333–335 (2002)
127. M.C. Benjamin, C. Wang, R.F. Davis, R.J. Nemanich, Observation of a negative electron affinity for heteroepitaxial AlN on α(6 h)-SiC(0001). Appl. Phys. Lett. **64**(24), 3288–3290 (1994)
128. C. Wu, A. Kahn, Negative electron affinity and electron emission at cesiated GaN and AlN surfaces. Appl. Surf. Sci. **162–163**, 250–255 (2000)
129. S. Uchiyama, Y. Takagi, M. Niigaki, H. Kan, H. Kondoh, GaN-based photocathodes with extremely high quantum efficiency. Appl. Phys. Lett. **86**(10) (2005)
130. J. Brown, J. Matthews, S. Harney, J. Boney, J. Schetzina, J. Benson, K. Dang, T. Nohava, W. Yang, S. Krishnankutty, High-sensitivity visible-blind AlGaN photodiodes and photodiode arrays. MRS Proc. **595**, 1 (1999)
131. J. Brown, J. Matthews, S. Harney, J. Boney, J. Schetzina, J. Benson, K. Dang, T. Nohava, W. Yang, S. Krishnankutty, Visible-blind UV digital camera based on a 32x32 array of GaN/AlGaN p-i-n photodiodes. MRS Internet J. Nitride Semicond. **4** (1999)
132. Status of AlGaN based focal plane arrays for UV solar blind detection **5964** (2005)
133. G. Mazzeo, J.-L. Reverchon, J. Duboz, A. Dussaigne, AlGaN-based linear array for UV solar-blind imaging from 240 to 280 nm. IEEE Sens. J. **6**, 957–963 (2006)
134. P.E. Malinowski, J.-Y. Duboz, P. De Moor, J. John, K. Minoglou, P. Srivastava, H. Abdul, M. Patel, H. Osman, F. Semond, E. Frayssinet, J.-F. Hochedez, B. Giordanengo, C. Van

Hoof, R. Mertens, Backside illuminated AlGaN-on-Si UV detectors integrated by high density flip-chip bonding. Physica Status Solidi (C) **8**(7–8), 2476–2478 (2011)

135. E. Cicek, R. McClintock, C. Cho, B. Rahnema, M. Razeghi, $Al_xGa_{1-x}N$-based solar-blind ultraviolet photodetector based on lateral epitaxial overgrowth of AlN on Si substrate. Appl. Phys. Lett. **103**(18), 181113 (2013)
136. K.C. Kim, Y.M. Sung, I.H. Lee, C.R. Lee, M.D. Kim, Y. Park, T.G. Kim, Visible-blind ultraviolet imagers consisting of 8 × 8 AlGaN p-i-n photodiode arrays. J. Vac. Sci. Technol., A **24**(3), 641–644 (2006)
137. J. Long, S. Varadaraajan, J. Matthews, J. Schetzina, UV detectors and focal plane array imagers based on AlGaN p-i-n photodiodes. Opto-Electron. Rev. **10**(4), 251–260 (2002)
138. R. McClintock, K. Mayes, A. Yasan, D. Shiell, P. Kung, M. Razeghi, 320x256 solar-blind focal plane arrays based on $Al_xGa_{1-x}N$. Appl. Phys. Lett. **86**(1) (2005)
139. First demonstration and performance of AlGaN based focal plane array for deep-UV imaging **7474** (2009)
140. E. Cicek, Z. Vashaei, E.K.-W. Huang, R. McClintock, M. Razeghi, $Al_xGa_{1-x}N$-based deep-ultraviolet 320 × 256 focal plane array. Opt. Lett. **37**(5), 896–898 (2012)
141. E. Cicek, R. McClintock, Z. Vashaei, Y. Zhang, S. Gautier, C.Y. Cho, M. Razeghi, Crack-free AlGaN for solar-blind focal plane arrays through reduced area epitaxy. Appl. Phys. Lett. **102**(5) (2013)
142. E. Michael, N. C. J, III-V direct-bandgap semiconductor optical filter. 11 (1981)
143. H.M. Manasevit, Epitaxial composite and method of making. 1 (1983)
144. K.M. ASIF, S.R.G, and S.R.A, UV detector and method for fabricating it. 4 (1986)
145. K.M. Asif [US], S.R.G [US], S.R.A [US], Tunable cut-off UV detector based on the aluminum gallium nitride material system. 9 (1986)
146. K.M. Asif [US], S.R. G [US], UV photocathode using negative electron affinity effect in $Al_xGa_{1-x}N$. 10 (1986)
147. S.W.H [US], Interference filter design using flip-flop optimization. 5 (1987)
148. H. Kai-Feng [CN], J.J.L [US], M.J.S. L [US], T. Kuochou [US], Quantum well vertical cavity laser. 3 (1991)
149. I. Toshihide [JP], O. Yasuo [JP], H. Ako [JP], Semiconductor light-emitting diode and method of manufacturing the same. 4 (1991)
150. L. Sergey [US], X. Ya-Hong [US], Vertical cavity semiconductor laser with lattice-mismatched mirror stack. 4 (1991)
151. K.P. C [AU], Current injection laser. 9 (1991)
152. S.J. Hwan, Semiconductor element for detecting ultraviolet rays at constant reliability and manufacturing method thereof. 12 (2004)
153. N. Katsuhiko, T. Toshiyuki, Ultraviolet ray detector. 5 (2006)
154. S. Charles [HK], Ultraviolet detector. 12 (2006)
155. W. Tilman [DE], T. Christoph [DE], L. Stefan [DE], H. Oliver [DE], K. H. Georg [DE], S. Sebastian [DE], S. Stephan [DE], Semiconductor component, electronic component, sensor system and method for producing a semiconductor component. 8 (2002)
156. S. Mayo [JP], T. Kohsuke [JP], G. Shunsuke [JP], K. Yasube [JP], E. Haruyuki [JP], H. Tatsuo [JP], I. Fukunori [JP], O. Eriko [JP], Photovoltaic ultraviolet sensor. 6 (2007)
157. K. Satoshi [JP], A. Hiroshi [JP], Nitride semiconductor substrate production method thereof and semiconductor optical device using the same. 2 (2005)
158. S.R. P [US], S.S. T [US], P.J. W [US], Dielectric passivation for semiconductor devices. 11 (2005)
159. J.M. Van Hove, J.N. Kuznia, D.T. Olson, M.A. Khan, M.C. Blasingame, High responsivity ultraviolet gallium nitride detector. 12 (1993)
160. T. Tadao, Semiconductor optical sensor. 6 (2000)
161. C. Qisheng [US], Schottky barrier detectors for visible-blind ultraviolet detection. 8 (2000)
162. D.M. Philip [US], E.N. Andrea [US], C. Kanin [US], Homoepitaxial gallium nitride based photodetector and method of producing. 2 (2005)

163. S. Katsumi [JP], I. Masayuki [JP], Y. Takafumi [JP], Backside-illuminated photodiode array, method for manufacturing same, and semiconductor device. 8 (2005)
164. H. Hikari, K. Satoshi, A. Hiroshi, A. Isamu, GaN-based compound semiconductor light receiving element. 9 (2005)
165. O. Ryota, D. Toru, Photoelectric conversion element, and its manufacturing method. 3 (2008)
166. F. Junichi [JP], O. Daisuke [JP], M. Kikuo [JP], N. Kenichi [JP], O. Keishi [JP], Photodiode, optical communication device, and optical interconnection module. 6 (2008)
167. K.K. Hamamatsu Photonics, Hamamatsu develops a new, highly sensitive GaN photocathode for UV detection (2010)
168. K.K. Hamamatsu Photonics, Photocathode technology (2014)
169. Y.-H. Lai, W.-Y. Cheung, S.-K. Lok, G. K. L. Wong, S.-K. Ho, K.-W. Tam, I.-K. Sou, Rocksalt mgs solar blind ultra-violet detectors. AIP Adv. **2**(1) (2012)
170. S.I. Keong [CN], L.Y. Hoi [CN], L.S. Kin [CN], C.W. Yip [CN], W.G.K. Lun [CN], T.K. Weng [CN], H.S. Kam [CN], Mgs solar-blind UV radiation detector. 12 (2012)
171. F. Junichi [JP], N. Takahiro [JP]
172. Jenoptik Polymer Systems GmbH, Data sheet epd-440-0-1.4 (2014)
173. K.K. Hamamatsu Photonics, Data sheet r759 (2014)
174. sglux GmbH, Data sheet tw30sx (2014)
175. J. Sun, F.-J. Liu, H.-Q. Huang, J.-W. Zhao, Z.-F. Hu, X.-Q. Zhang, Y.-S. Wang, Fast response ultraviolet photoconductive detectors based on Ga-doped ZnO films grown by radio-frequency magnetron sputtering. Appl. Surf. Sci. **257**(3), 921–924 (2010)
176. D.K. Wickenden, Z. Huang, D.B. Mott, P.K. Shu, Development of gallium nitride photoconductive detectors. Johns Hopkins APL Technical Digist **18**(2) (1997)
177. ITME - Institute of Electronic Materials Technology Poland, Catalog of 2010 (2010)
178. IL-Metronic Sensortechnik GmbH, Data sheet UVD 370 (2014)
179. Jenoptik Polymer Systems GmbH, Prototype data sheet epd-260-1.0 (2014)
180. Genicom, Data sheet GUVC-T10GD-L (2014)
181. L. Jian-Fei, H. Ze-Qiang, Z. Wen-Le, J. Hao, Large active area AlGaN solar-blind schottky avalanche photodiodes with high multiplication gain. Chin. Phys. Lett. **30**(3), 037803 (2013)
182. Jenoptik Polymer Systems GmbH, Data sheet epd-270-0-0.3-1 (2014)
183. IFW Optronics, Data sheet jec 1c (2014)